Università degli studi di Padova

Dipartimento di Fisica e Astronomia "Galileo Galilei"
Istituto di Fotonica e Nanotecnologie di Padova

Corso di Laurea Magistrale in Fisica

Tesi di Laurea

Adaptive Optical Microscopy using the Pupil Segmentation

Relatore:
Prof. Stefano Bonora

Correlatore:
Dott. Martino Quintavalla

Laureando:
Tommaso Furieri

Anno Accademico 2018-2019

ACKNOWLEDGMENTS

Tra le persone che vorrei ringraziare ci sono sicuramente il Dr. Stefano Bonora, relatore di questo lavoro di tesi, che ha messo a dispozione il suo tempo e conoscenze, nonchè il laboratorio di ottica adattiva dove ho speso gran parte del tempo di svolgimento di questa tesi, e il Dr. Martino Quintavalla, correlatore e prezioso sostegno pratico che mi ha assistito in laboratorio e non solo.

Un ringraziamento poi va a tutti i miei compagni e amici di università, con i quali ho condiviso momenti di studio e di svago e che sono riusciti a sopportarmi in tutti questi anni

Non posso dimenticare poi i miei amici di vita, che mi hanno sempre sostenuto e accompagnato in questo percorso, soprattutto Luana e il suo infaticabile e insostituibile sostegno in tutti questi mesi.

Ringrazio inoltre i miei familiari, zii e cugini di ogni grado.

Infine, ma sicuramente non per importanza, ringrazio i miei fratelli Nicola e Leonardo, insostituibili compagni di avventura e di vita, e i miei instancabili genitori Francesco e Marilena, che mi hanno sempre supportato in tutto e per tutto e ai quali un semplice grazie non basta.

"Egli fa vedere ciò che vuole e come vuole
perchè possiede l'essenziale dei segreti dell'ottica.
È quest'Arte... che ha trovato il modo di far uscire echi visivi dal cristallo
e di avvicinare gli oggetti più lontani.
È quest'Arte ingannevole che si prende gioco degli occhi e sconvolge tutti i sensi."

Charles Patin

CONTENTS

INTRODUCTION

Microscopy is a relatively old field. It's birth is dated back in 17^{th} century and has continuously grown till recent days where scientists are able to achieve sub diffraction limited results. However in some cases aberrations are inevitable, for example because of sample inhomogeneities and refractive index mismatch.

The role of Adaptive Optics is to locally remove or reduce this aberration modifying the phase of the incoming light using a deformable device and a measurement and control system.

While this idea dates back in 1953 [7] the real practical use was found in astronomy, around the 90′, where the main source of aberration comes from atmospheric turbulence with a fast variation frequency ($\geqslant$ 100Hz). The most common devices used in astronomy are deformable mirrors and, for the wavefront measurement, the Shack-Hartmann wavefront sensor having the good property of a very slow response time.

Conversely, in microscopy the aberrations are usually stationary. This brought scientists to use alternative approaches, like sensor-less algorithms that indirectly corrects for aberrations by maximizing a metric usually function of the image intensity.

While this approach has the advantage of a simplification of the optical path, it is usually slow and does not permit to measure the aberration. This is a problem especially when dealing with fluorescent specimen when the prolonged exposition to light can bring to the photobleacing of the fluorescent molecules. Another recent approach that can overcome the slow correction time of a sensorless approach and that can measure the wavefront without the use of a wavefront sensor is the Pupil Segmentation technique [11] where the pupil of the system is divided into subapertures, each of them producing an image of the sample. From the relative shifts between all the images it is possible to reconstruct the wavefront of the image and correct for it using an adaptive optics device.

A recent new kind of device that is finding applications in different adaptive optics systems, are adaptive lenses. Clearly the main advantage of an adaptive lens over a deformable mirror, is the fact that the optical path does not need to be folded, and the installation in an optical system such as a telescope or a microscope can be less invasive.

In microscopy, one of the most common aberrations that can be found in the study of biological samples is Spherical aberration. This aberration arises when the specimen and the immersion fluid refractive indexes are not perfectly matched and, as we will see later, especially with high numerical aperture (NA) objectives.

This problem is reflected in various applications related to the use of an optical system such as optical trapping or micro-fabrication in transparent materials.

The aim of this thesis work is to have an in-depth look at the spherical aberration problem and test an adaptive lens to use in the correction of aberrations in the case of a real microscopic setup using the Pupil Segmentation technique in conjunction of an adaptive lens.

My work will be articulated in this way:

In the **FIST PART** I will give a brief introduction to the main theoretical concepts. in particular the first chapter is about microscopy and the modern formulation of optics. I will then introduce in chapter 2 a formalism to define aberrations in an optical system, primarily focusing on the spherical aberration problem in microscopy, and in the following chapter some elements of Adaptive Optics (AO) applied to microscopy will be presented.

In the **SECOND PART** the experimental results will be shown. In the fourth chapter I will discuss the characterization of the objectives to my disposal and the measurements and correction of an induced spherical aberration, aimed at the reproduction of a typical situation in biological microscopy, using an adaptive lens. In the following chapter I will expose the implementation of the pupil segmentation wavefront measurement in conjunction with an adaptive lens to correct for aberrations in a bright field microscope and in the seventh chapter are presented the results of the pupil segmentation corrective module in a light sheet microscope.

Part I.

Elements of Microscopy and Adaptive Optics

1 ELEMENTS OF OPTICAL MICROSCOPY

1.1 AN HISTORICAL INTRODUCTION OF OPTICS

While we have some traces of the first optical concepts and ideas already in the years before Christ, we need to wait until the 17^{th} century to see the first real telescope invented by Hans Lippershey followed by Galileo Galilei few months later.

In the same years the first microscope was designed, probably by Zacharias Janssen, and the first theoretical optical principles was discovered. Among these, we need to underline the law of refraction (Snell Law) and the first observation of interference.

At the time, the common belief was that light was composed of particles traveling in space and the discover of an ondulatory nature of light was not commonly accepted mainly because the difficulty in explaining geometric optics in an ondulatory way.

We need to wait until 1678 with the wave theory of light written by Huygens to have a good explanation of the rectilinear propagation of light. In fact we can consider the propagated wavefront as the sum of spherical wavelets generated at any sub-sequential time. This is called now the *Huygens-Fresnel Principle* in honor of Fresnel, who merged the Huygens ideas with the diffraction principles; in fact the sum must consider the amplitude and relative phases of every wavelet.

$$U(P) = U_0 \frac{e^{ikr_0}}{r_0} \int_\Sigma \frac{e^{iks}}{i\lambda s} \frac{1-\cos(\theta)}{2} d\Sigma \tag{1.1}$$

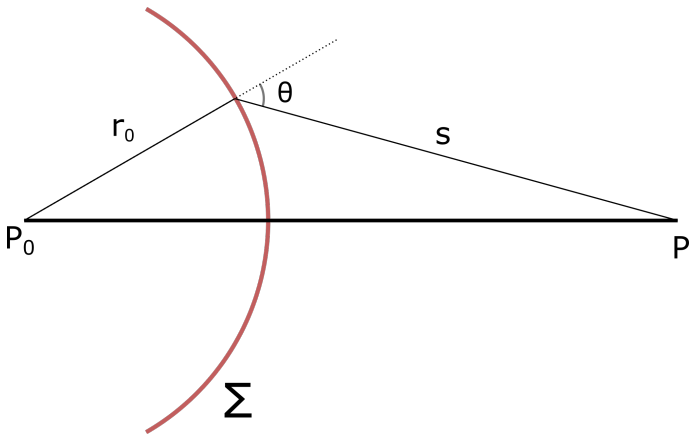

Figure 1.1.: Schematic representation of the Huygens-Fresnel equation in the case of the propagation of a spherical wavefront

At this point, the scientific community was convinced by the fact that the speed of light was finite and, in later years with Maxwell, that light was an electromagnetic wave traveling at speed c (in a medium called ether).

A new era started in 1905 with Einstein and Poincare and the experiment of Michelson-Morley. In a bunch of years the idea of ether was discarded, the speed of light became a constant in every reference system and the corpuscular and wave nature of light became a duality.

To assist a new rebirth of optics we must wait until the second part of the 20^{th} century. In this period optics was approached in a totally new way with the new mathematical formalism of Fourier analysis. This, accompanied with the technical improvements made possible to design and build complex and diffraction limited systems and, with the study and development of new techniques, sub diffraction limited microscopes.

1.2 MODERN OPTICS AND IMAGE FORMATION

In this section we will see in the most concise way, the principal results of modern optics and their application in the process of the image formation. All these results are well known, and a more complete and rigorous exposition can be found in [1][2].

1.2.1 Diffraction Integrals

Equation 1.1, can be written for the general case of a clear aperture A:

$$\mathcal{U}(x,y,z) = \int_{-\infty}^{+\infty}\int_{-\infty}^{+\infty} \mathcal{U}_{in}(\xi,\eta,0)\mathcal{T}_A(\xi,\eta)\frac{e^{iks}}{i\lambda s}\cos(\theta)\,d\xi\,d\eta \tag{1.2}$$

where $\mathcal{T}_A$ is the transmission function

$$\mathcal{T}_A(\xi,\eta) = \begin{cases} 1 & \text{if we are inside the aperture} \\ 0 & \text{if we are outside the aperture} \end{cases}$$

and $\cos(\theta) = z/s$

The first approximation we can do, is to expand:

$$\begin{aligned} s &= \sqrt{(x-\xi)^2 + (y-\eta)^2 + z^2} \\ &= z\sqrt{\left(\frac{x-\xi}{z}\right)^2 + \left(\frac{y-\eta}{z}\right)^2 + 1} \\ &\simeq z + \frac{1}{2z}\left[(x-\xi)^2 + (y-\eta)^2\right] \end{aligned}$$

the field is now:

$$\mathcal{U}(x,y,z) \simeq z\frac{e^{ikz}}{i\lambda}\int_{-\infty}^{+\infty}\int_{-\infty}^{+\infty} \mathcal{U}_{in}(\xi,\eta,0)\mathcal{T}_A(\xi,\eta)\frac{e^{\frac{ik}{2z}\left[(x-\xi)^2+(y-\eta)^2\right]}}{(x-\xi)^2+(y-\eta)^2+z^2}\,d\xi\,d\eta$$

if we neglect the all the terms except z^2 in the denominator we obtain the **Fresnel diffraction integral**.

$$\boxed{\mathcal{U}(x,y,z) \simeq z\frac{e^{ikz}}{i\lambda}\int_{-\infty}^{+\infty}\int_{-\infty}^{+\infty}\mathcal{U}_{in}(\xi,\eta,0)\mathcal{T}_A(\xi,\eta)e^{\frac{ik}{2z}\left[(x-\xi)^2+(y-\eta)^2\right]}\,d\xi\,d\eta} \tag{1.3}$$

From this formula, we can expand the squares in the exponential. Imposing the Fraunholfer approximation:

$$\frac{\xi^2+\eta^2}{\lambda z} << 1 \tag{1.4}$$

we obtain the **Fraunholfer diffraction integral**

$$\boxed{\mathcal{U}(x,y,z) \simeq z\frac{e^{ikz}}{i\lambda z}e^{\frac{ik}{2z}(x^2+y^2)}\int_{-\infty}^{+\infty}\int_{-\infty}^{+\infty}\mathcal{U}_{in}(\xi,\eta,0)T_A(\xi,\eta)e^{-i\frac{2\pi}{\lambda z}(x\xi+y\eta)}\,d\xi\,d\eta} \tag{1.5}$$

1.2.2 The Angular Spectrum

As already said, modern optics uses the Fourier Formalism.
Let's consider a complex wave field $\mathcal{U}(x,y,z)$ at a given wavelength λ propagating in the $\hat{z}$ direction. We can obtain the spectrum of $\mathcal{U}$ evaluated at $z=0$ by the means of a Fourier transform:

$$\mathcal{A}(f_x,f_y,0) = \mathfrak{F}\left[\mathcal{U}(x,y,0)\right] = \int_{-\infty}^{+\infty}\int_{-\infty}^{+\infty}\mathcal{U}(x,y,0)e^{-2\pi i(f_x x+f_y y)}\,dx\,dy \tag{1.6}$$

This expression can be interpreted as a superposition of linear phase exponentials, each of that correspond to a plane wave crossing the xy plane and propagating in the directions of $\vec{k}$ with directions cosines

$$\begin{aligned}\alpha &= \lambda f_x\\ \beta &= \lambda f_y\\ \gamma &= \sqrt{1-(\lambda f_x)^2-(\lambda f_y)^2} = \sqrt{1-\alpha^2-\beta^2}\end{aligned}$$

$\mathcal{A}(f_x,f_y,0)$ is called the **Angular Spectrum** of the field $\mathcal{U}(x,y,0)$

If now we want see what happens to the field $\mathcal{U}$ at various distances z, we remember that it can always been written as the inverse Fourier transform of its angular spectrum, namely:

$$\mathcal{U}(x,y,z) = \mathfrak{F}^{-1}\left[\mathcal{A}(f_x,f_y,z)\right] = \int_{-\infty}^{+\infty}\int_{-\infty}^{+\infty}\mathcal{A}(f_x,f_y,z)e^{2\pi i(f_x x+f_y y)}\,df_x\,df_y \tag{1.7}$$

moreover $\mathcal{U}$ must satisfy Helmholtz Equation

$$\nabla^2\mathcal{U}+k^2\mathcal{U}=0 \tag{1.8}$$

It can be seen, that a solution is given by:

$$\mathcal{A}(f_x, f_y, z) = \mathcal{A}(f_x, f_y, 0)e^{i\mu z} \tag{1.9}$$

where

$$\mu = k\gamma$$

So the propagation only affect the phase of the various components of the angular spectrum. It has to be underlined that there are two distinct cases when the argument of the square root in γ is positive or negative; i.e. if

$$f_x^2 + f_y^2 < 1/\lambda^2$$

or

$$f_x^2 + f_y^2 < 1/\lambda^2$$

The second case correspond to the case of the evanescent wave, a consequence of the fact that the electromagnetic field cannot be discontinuous at a boundary.
In practice this waves decays in the range of the order of λ, so for our purpose are of no interest.

Finally the field $\mathcal{U}(x, y, z)$ can be computed using the Fourier transform

$$\mathcal{U}(x, y, z) = \mathfrak{F}^{-1}\left[\mathcal{A}(f_x, f_y, z)\right] = \mathfrak{F}^{-1}\left[\mathcal{A}(f_x, f_y, 0)e^{i\mu z}\right].$$

We can now show how the angular spectrum is affected if we place a diffracting structure, like an aperture, a sample etc. In general, the field $\mathcal{U}(x, y, 0)$ just after the diffracting structure, can be written as

$$\mathcal{U}(x, y, 0) = \mathcal{U}_{in}(x, y, 0)\mathcal{T}(x, y)$$

where $\mathcal{U}_{in}$ is the incoming field just before the diffracting structure, and $\mathcal{T}$ is it's transmittance function that in general can be composed of two terms:

$$\mathcal{T}(x, y) = T(x, y)e^{i\phi(x,y)} \tag{1.10}$$

the first one is real and spans from 0 to 1 to take into account for the loss of intensity (called apodization) multiplied by the second one, corresponding to a phase shift.

The angular spectrum just after the diffracting structure can be found by Fourier transforming $\mathcal{U}(x, y, 0)$ (remembering the convolution properties of the Fourier transform[1]):

$$\mathcal{A}(f_x, f_y, 0) = \mathfrak{F}[\mathcal{U}(x, y, 0)] = \mathfrak{F}[\mathcal{U}_{in}(x, y, 0)\mathcal{T}(x, y)] = \mathfrak{F}[\mathcal{U}_{in}(x, y, 0)] \circledast \mathfrak{F}[\mathcal{T}(x, y)]$$

so

$$\mathcal{A}(f_x, f_y, 0) = \mathcal{A}_{in}(f_x, f_y, 0) \circledast \mathcal{A}_T(f_x, f_y)$$

If we consider a plane wave with amplitude A, $\mathcal{A}_{in}$ becomes:

$$\mathcal{A}_{in}(f_x, f_y, 0) = A\,\delta(f_x, f_y)$$

and then

$$\boxed{\mathcal{A}(f_x, f_y, 0) = A \cdot \mathcal{A}_T(f_x, f_y)} \tag{1.11}$$

So the angular spectrum only depends by the aperture (and the amplitude of the incoming wave) and can be computed by Fourier transforming the transmittance function.

1 We denote the convolution operation with this symbol: $\circledast$

1.2.3 Abbe Theory of Image Formation

When we are dealing with optical systems, the transmittance function of the system, shown in 1.10, is called **generalized pupil function**. We denote it with this notation:

$$\mathcal{P}(\xi,\eta) = T(\xi,\eta)e^{i[\phi_L(\xi,\eta)+\phi_A(\xi,\eta)]}$$

Where we separated the contribution of the phase imparted by a perfect lens (ϕ_L) to the contribution of the aberrations (ϕ_A).

In the simple case of a spherical thin lens, in the paraxial approximation the ϕ_L term becomes:

$$\phi_L(\xi,\eta) = -\frac{k}{2f}(\xi^2+\eta^2) \tag{1.12}$$

where

$$\frac{1}{f} = \frac{1}{R}(n_L - 1)$$

n_L is the refractive index of the lens and R is the radius of the spherical surface and $\phi_A = 0$. If from the generalized pupil function, we exclude the phase imparted by the lens, we obtain the **pupil function** of the lens:

$$P(\xi,\eta) = T(\xi,\eta)e^{i\phi_A(\xi,\eta)} \tag{1.13}$$

So we can consider a lens as a phase transformer of the input field.

We see now what happens to a diffracting structure (object) coherently illuminated and placed before the lens at a distance d. The field emerging from the object has a spectrum:

$$\mathcal{A}_O(f_X,f_Y) = \mathfrak{F}(\mathcal{U}_O(X,Y,-d))$$

we can now propagate it to the lens using the 1.9 and obtain the field incident on the lens by anti-transforming the propagation of the angular spectrum. We can now propagate it to the focal point of the lens using the Fresnel diffraction integral 1.3 obtaining:

$$\boxed{\mathcal{U}(x,y) = \frac{1}{i\lambda f}e^{\frac{ik}{2f}(1-\frac{d}{f})(x^2+y^2)}\mathcal{A}_O(f_X,f_Y)} \tag{1.14}$$

We can now see two important cases:

- **Object near the lens**
  In this case $d = 0$ and we obtain:

  $$\mathcal{U}(x,y) = \frac{1}{i\lambda f}e^{\frac{ik}{2f}(x^2+y^2)}\mathcal{A}_O(f_X,f_Y)$$

  In practice this is the Fraunhofer diffraction pattern obtained in the focal plane of the lens.

- **Object in the focal point of the lens**
  In this case $d = f$ and we obtain:

  $$\mathcal{U}(x,y) = \frac{1}{i\lambda f}\mathcal{A}_O(f_X,f_Y)$$

that is the exact Fourier transform of the object obtained in the back focal plane of the lens.

To end this section, we want to see how an optical imaging system respond at a distance d_i in the image space when a point source is located at a distance d_o in the object space.

To do so, we can represent our optical device as a linear operator acting on the light coming from the object space to form an image in the image space.

In this context, we define $g(x, y, X, Y) = S(\delta(x' - X, y' - Y))$ as the response of the system in the point (x, y) to a delta function located at (X, Y) (point source).

This is called the amplitude **point spread function** (PSF) of the system that we denote as $g(x, y, X, Y)$ where X, Y are the coordinates in the object space, and x, y are the coordinate in the image space. In general, if we assume that our system is spatial invariant, $g(x, y, X, Y)$ depends only by the distance $(X - x, Y - y)$.

The image then will be:

$$\boxed{\mathcal{U}_i(x, y) = \int_{-\infty}^{+\infty}\int_{-\infty}^{+\infty} \mathcal{U}_o(X, Y) g(x - X, y - Y)\, dX dY = U_o \circledast g} \tag{1.15}$$

so the amplitude of the image field is the convolution of the amplitude of the diffracted object field with the PSF of the system.

It can be shown that, if the lens law is satisfied, the PSF has the following form:

$$g(x, y, X, Y) = \int_{-\infty}^{+\infty}\int_{-\infty}^{+\infty} P(\xi, \eta) e^{-2\pi i\left[\left(\frac{x}{\lambda d_i} + \frac{X}{\lambda d_o}\right)\xi + \left(\frac{y}{\lambda d_i} + \frac{Y}{\lambda d_o}\right)\eta\right]} d\xi d\eta \tag{1.16}$$

that is the Fourier transform of the pupil function of the lens.

2 ABERRATIONS

We define the wavefront of a monochromatic wave as the set of all points in space that have she same phase (so for our interests the wavefront is a surface).

In an ideal imaging system, the field emerging from a point source is focused to a point in the image space, so the emerging wavefront from the lens is spherical.

Aberrations are a deviation of the wavefront from the reference one. This deviation is in general not constant and depends on the position (ξ, η). We can write the aberration term of the wavefront incident on the pupil function 1.13 as:

$$e^{i\phi_A(\xi,\eta)} = e^{i2\pi W(\xi,\eta)} \tag{2.1}$$

and we call $W(\xi, \eta)$ the **aberration function** measured in unit of wavelength.

From 1.16 we notice that this aberration term will impact on the PSF of the system via the pupil function. So the image formed will be degraded and with a lower resolution.

It is often useful to have a value that can tell the average error of an aberrated wavefront. We define the root mean square wavefront error W_{RMS} as:

$$W_{RMS} = \sqrt{\frac{1}{S_A}\int_A W^2(\xi,\eta)\, d\xi d\eta} \tag{2.2}$$

Where A is the aperture in which we integrate and S_A it's surface area.

Given the fact that we are usually dealing with apertures with circular symmetries, we change the lens coordinates into polar with the usual convention:

$$\xi = \rho\cos\theta$$
$$\eta = \rho\sin\theta$$

In general we could expand the aberration function with a series of polynomials. An useful expansion is given by the Zernike polynomials

2.1 ZERNIKE POLYNOMIALS

Zernike polynomials are a set of functions defined over the unit circle that have the good property of being orthogonal.

Their name is in honor of the physicist Frits Zernike, winner of the 1953 Nobel Prize in Physics and are widely used in many optical fields.

In general we can reconstruct the aberration function of the system using a linear combination of Zernike polynomials in this way:

$$W(\rho,\theta) = \sum_{n,m}^{\infty,\infty} c_{n,m} Z_m^m(\rho,\theta) \tag{2.3}$$

Where Z_n^m are the Zernike polynomials, $c_{n,m}$ are the weights of the polynomials, called Zernike coefficients, n, m are integers with the constrain

$$\begin{aligned} n &\geqslant 0 \\ |m| &\leqslant n \\ n - m &\in 2\mathbb{N} \end{aligned}$$

and ρ, θ are the radial and and azimuthal coordinates.

The explicit formulation of Z_n^m is given by:

$$Z_n^m(\rho,\theta) = \left[\frac{2(n+1)}{1+\delta_{m0}}\right]^{1/2} R_n^m(\rho)\cos(m\theta) \tag{2.4}$$

R_n^m is the radial part given by:

$$R_n^m(\rho) = \sum_{s=0}^{(n-m)/2} \frac{(-1)^s (n-s)!}{s!(\frac{n+m}{2}-s)!(\frac{n-m}{2}-s)!}\rho^{n-2s} \tag{2.5}$$

and the normalization is $\int_0^{2\pi}\int_0^1 Z_n^m(\rho,\theta)Z_n^m(\rho,\theta)\rho d\rho d\theta = \pi$.

Here we show the first four orders of Zernike polynomials with their associated aberrations and shapes.

As already said, one of the most useful properties of the Zernike polynomials is their orthogonality over the unit circle.
In fact one can check that:

$$\int_0^{2\pi}\int_0^1 Z_n^m(\rho,\theta)Z_{n'}^{m'}(\rho,\theta)\rho d\rho d\theta = \delta_{nn'}\delta_{mm'} \tag{2.6}$$

If we have the explicit formula of $W(\rho,\theta)$ we can obtain the Zernike coefficients integrating over the unit circle:

$$c_{n,m} = \frac{1}{\pi}\int_0^1\int_0^{2\pi} W(\rho,\theta)Z_n^m(\rho,\theta)\rho d\rho d\theta \tag{2.7}$$

In the special case we are dealing with radial aberrations only ($W(\rho)$), we can set $m = 0$ and use the orthogonality relation to obtain the Zernike coefficients:

$$\begin{aligned} m &= 0 \\ R_n^0(\rho) &= \sum_{s=0}^{n/2} \frac{(-1)^s (n-s)!}{s!(\frac{n}{2}-s)!^2}\rho^{n-2s} \\ Z_n^0(\rho) &= \sqrt{n+1}R_n^0(\rho) \\ c_{n0} &= 2\int_0^1 W(\rho)Z_n^0(\rho)\rho d\rho \end{aligned}$$

n	m	Z_n^m	Name
0	0	1	Piston
1	−1	$2\rho\sin\theta$	Tilt
	1	$2\rho\cos\theta$	Tip
2	−2	$\sqrt{6}\rho^2\sin 2\theta$	Oblique Astigmatism
	0	$\sqrt{3}(2\rho^2-1)$	Defocus
	2	$\sqrt{6}\rho^2\cos 2\theta$	Vertical Astigmatism
3	−3	$\sqrt{8}\rho^3\sin 3\theta$	Vertical Trefoil
	−1	$\sqrt{8}(3\rho^3-2\rho)\sin\theta$	Vertical Coma
	1	$\sqrt{8}(3\rho^3-2\rho)\cos\theta$	Horizontal Coma
	3	$\sqrt{8}\rho^3\cos 3\theta$	Vertical Trefoil
4	−4	$\sqrt{10}\rho^4\sin 4\theta$	Oblique Quadrafoil
	−2	$\sqrt{10}(4\rho^4-3\rho^2)\sin 2\theta$	Oblique Secondary Astigmatism
	0	$\sqrt{5}(6\rho^4-6\rho^2+1)$	Primary spherical
	2	$\sqrt{10}(4\rho^4-3\rho^2)\cos 2\theta$	Vertical Secondary Astigmatism
	4	$\sqrt{10}\rho^4\cos 4\theta$	Vertical Quadrafoil

Table 2.1.: First four orders of Zernike Polynomials

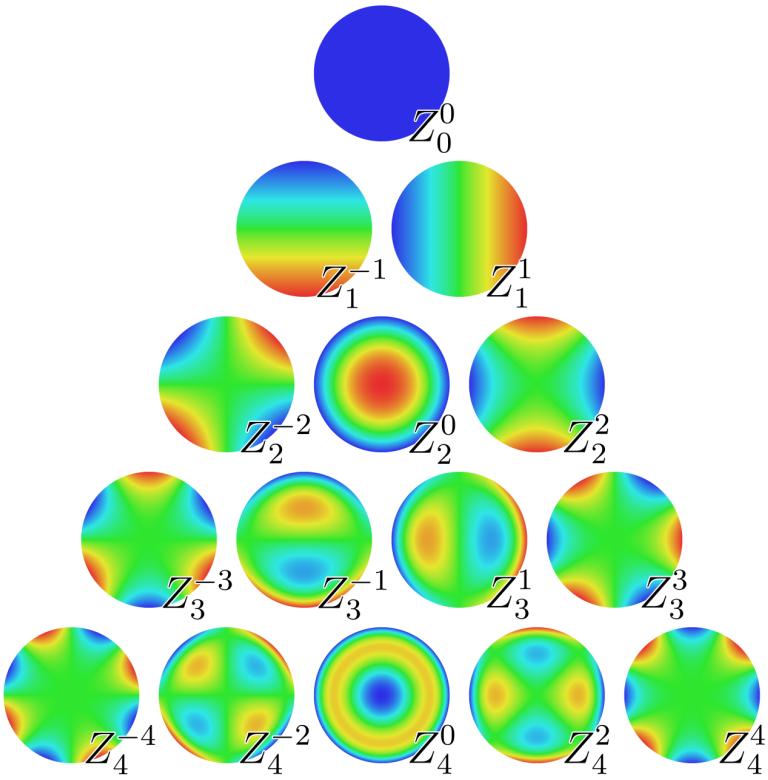

Figure 2.1.: Plot of the first four orders of Zernike polynomials

It is easy to show that thanks to the orthogonality, once we decompose the aberration function in Zernike polynomials, the root mean square wavefront error is:

$$W_{RMS} = \sqrt{\sum_{n,m} c_{n,m}^2} \tag{2.8}$$

2.1.1 Maréchal Criterion

One question that can arise is when our system can be said aberration free. To this purpose a criterion has been developed stating that

$$W_{RMS} < \frac{1}{14} \simeq 0.08 \tag{2.9}$$

in units of wavelengths.
This criterion is called "Maréchal Criterion" and, when satisfied, the system is said to be **diffraction Limited**.

This is of course a practical criterion, because the theoretical resolution limited by diffraction, in the case of microscopy, is given by the **Abbe Criterion**

$$d = \frac{\lambda}{2NA} \tag{2.10}$$

and any instruments can only approach this resolution.

2.2 SOURCES OF ABERRATION AND SPHERICAL ABERRATION IN MICROSCOPY

Aberration in a microscope can be imputed to different issues in two main categories:

- optical induced aberrations
  - a not well design optics (cheap and not well corrected objectives)
  - a bad alignment of the components
- sample induced aberrations
  - a mismatch in refractive index between the sample and the immersion medium
  - field dependent aberration

While the optical component of the aberration can be fixed using better optical components and with a more accurate alignment, the specimen induced aberration are more complex to deal with. In particular

2.2.1 Spherical Aberration in Microscopy

It is often the case in biological microscopy, that some refractive index mismatches are present: either inside the specimen there are some position dependent inhomogeneities of the refractive index (field component) or the design refractive index of the objective lens differ from the one of the sample, so the working immersion medium has a different refractive index compared to that of the specimen.

The direct consequence of the second, is the arise of spherical aberration[3], causing the illumination and/or the collection objective PSF to broaden with a consequential loss in signal and image sharpness. This problem reflect not also in the study of biological

samples, but also in all the applications where an optical system is used and a mismatch of the refractive index is present such as optical trapping[4] or micro-fabbrication in transparent materials.

It has been shown that a formula for the aberration function in the case of a mismatch in the refractive index of the imaged sample can be obtained analytically [5] (The derivation is covered in Appendix: Derivation of formula 2.11)):

$$W(\rho) = \frac{dNA}{\lambda}\left(\sqrt{\left(\frac{n_m}{NA}\right)^2 - \rho^2} - \sqrt{\left(\frac{n_d}{NA}\right)^2 - \rho^2}\right) \tag{2.11}$$

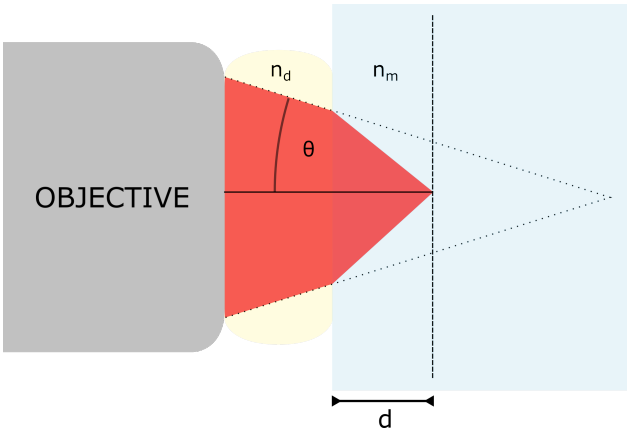

Figure 2.2.: Example of a light beam focused by an oil immersion objective ($n_d \simeq 1.52$) into an aqueous solution ($n_m \simeq 1.33$) at a depth d

In this equation ρ is the normalized pupil radius, n_d and n_m are the refractive index of the design immersion medium of the objective lens and the refractive index of the mismatched medium, d is the imaging depth inside the mismatched medium and NA is the **numerical aperture** of the objective lens defined as:

$$NA = n_d \sin\theta \tag{2.12}$$

where θ is the highest angle of acceptance of the light cone incident to the objective as it is shown in figure 2.2.

Using equation 2.7 we can obtain the Zernike coefficients of the aberration function. Given the fact that this expression depends only on ρ; m is equal to 0 and we can consider only the radial expansion (Defocus, Primary Spherical, Secondary Spherical...). One can show [6] that the main aberration is defocus, followed by primary spherical and the other spherical orders with decreasing magnitude. In particular it turns out that the most important terms are defocus and primary spherical aberration (SA), and clearly while the first one is easily correctable, the second one is the most problematic one.

Here we can see the dependence of W_{RMS} considering only the primary spherical aberration term of the expansion ($c_{4,0}$) on the different parameters in 2.11 in the case of an oil objective ($n_d \simeq 1.52$) focusing in water ($n_m \simeq 1.33$):

It is evident that SA has a linear dependency on focusing depth but a highly nonlinear dependency on the NA. In particular, high NA objectives ($NA > 1$) are the ones where the effect of SA is mostly pronounced.

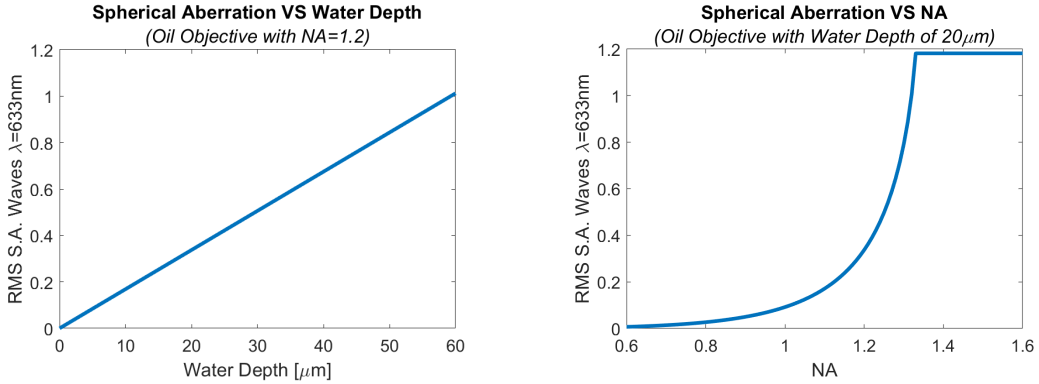

(a) (b)

Figure 2.3.: Dependency of Primary Spherical Aberration RMS on focusing depth 2.3a and NA of the Objective 2.3b

Last thing worth to be noted is that, looking at figure 2.3b, we can see starting from $NA = 1.33$ a stop in the increase of SA. This is because of Snell law.

From the definition of NA (eq. 2.12) the maximum angle of light incidence to the objective is

$$\theta = \arcsin\left(\frac{NA}{n_d}\right)$$

In the interface between the two medium with different refractive indexes, we can apply Snell Law

$$NA = n_d \sin\theta_d = n_m \sin\theta_m$$

From this we can see that NA is limited by n_m because $\sin\theta_m$ cannot be greater than 1. Finally the the maximum angle of acceptance is given by total internal reflection

$$\theta_{d,max} = \arcsin\left(\frac{n_m}{n_d}\right)$$

(a) (b)

Figure 2.4.: Graphical rays representation of spherical aberration when $NA < n_m$ (left) and $NA > n_m$ (right). In both cases $n_m < n_d$

A graphic representation of this can be found in figure 2.4 where a light beam is focused into a solution with a mismatched refractive index.

To the left we see the case where $n_m < n_d$ and $NA < n_m$ while to the right $n_m < n_d$ but $NA > n_m$ and outer rays are reflected back because of total internal reflection.

We can now explain the behavior of the curve in figure 2.3b when $NA > n_m$. In fact in this range NA remains constant, thus the aberration does not change.

3 ELEMENTS OF ADAPTIVE OPTICS

Adaptive Optics (AO) is a relatively recent technology used to correct for aberration in optical systems caused by a deformation of the wavefront.

3.1 ADAPTIVE OPTICS

AO was initially conceived by Babcock[7] in 1953, but only at the begin of 90' it was possible to build the first AO systems. AO is now applied to different scientific fields like astronomy where the aberrations are induced by atmospheric turbulence, and microscopy[8] where the non uniformities in the refractive index of the sample causes that the optical path is not uniform in every direction. This is reflected in a phase difference, hence in a deformation of the wavefront.

The main components of an AO system are:

- A **wavefront sensor**, used to measure the deviation of the wavefront from the reference one.
- A **deformable device** with the aim of introduce an optical path difference and thus modify the wavefront in a controlled way
- A **control system** that can control the deformable device taking in input the measures of the wavefront sensor.

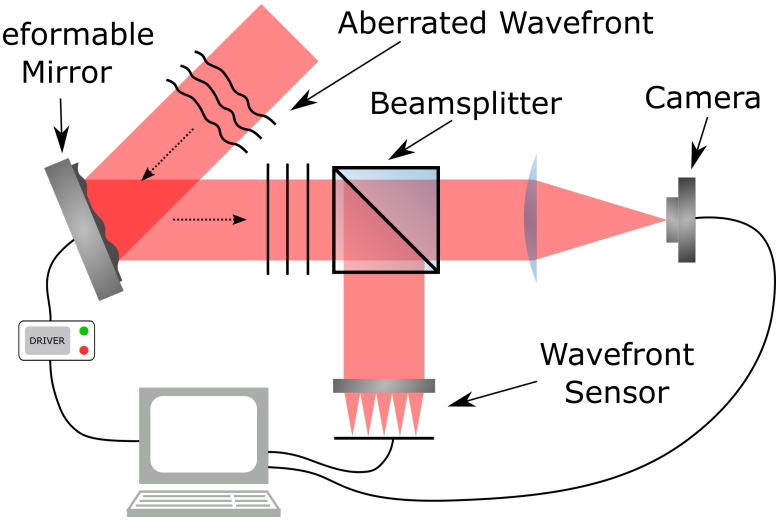

Figure 3.1.: Example of a typical Adaptive Optic setup

3.1.1 Wavefront Sensors

A wavefront Sensor (WS) is a device that, as the name already states, serves to measure the shape of a wavefront. There are many kind of wavefront sensors, like:

- Shack Hartman wavefront sensor
- Wavefront curvature sensor
- Shearing interferometer
- Pyramid wavefront sensor (developed by Roberto Ragazzoni in the university of Padova)
- Wavefront curvature sensor

and many others.

We focus in this section only on the Shack Hartman wavefront sensor, that is actually the most diffused one and a good example on how Slopes Wavefront Sensors works.

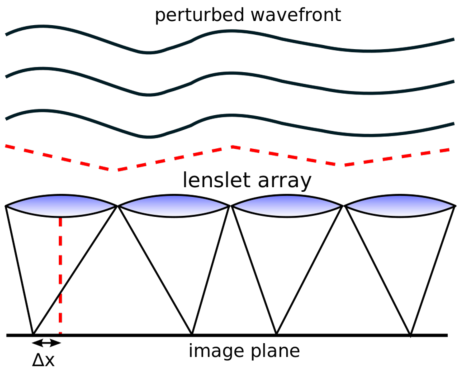

Figure 3.2.: Illustration of the Shack Hartman WS working principle

SH WS consist of a lenslet array, placed at the focal distance of the lenses away of a screen. If we consider a single lens of the lenslet array, we can approximate the portion of the wavefront incident on it lens as affected only by a local tip/tilt aberration. Therefore this will focus the local incoming wavefront to the screen forming an image of the object in a position shifted from the center of the lens axis.

The Object is usually a star (ideally a point source), thus the result in the screen (a camera sensor) are a number of spots equal to the number of lenses of the lenslet array, each one with it's own displacement. So one can record each displacement and gather the gradient of the wavefront evaluated for the position of every lens:

$$\nabla W|_{(x_i,y_i)} = \frac{\Delta_i}{f \cdot \lambda} \tag{3.1}$$

where x_i, y_i are the coordinates of the $i-th$ lenslet array lens, Δ_i is the displacement in the image plane due to the $i-th$ lenslet array lens, f is the focal length of the lenses of the array and λ is the wavelength of the incident light.

One the gradient of the wavefront is measured, it is not difficult to gather the wavefront itself from it.

Wavefront Rapresentation

There are more than one way to represent a wavefront W.

The simplest way is a 3D plot od a 2D plot using colors to delineate the depth. This representation has been already used in figure 2.1.

Another common way is to show the interferogram between an ideal flat wavefront and the wavefront in exam.

Calling W_0 the reference wavefront, we can set it to be constantly zero together with the piston term of W. This has no effect on the aberration but makes the formulation simpler.

In this way the interference intensity is just given by

$$I(x, y) = \sin^2\left(2\pi \frac{W(x, y)}{\lambda}\right) \tag{3.2}$$

and a fringe denotes a variation in the wavefront path of $\lambda/2$. I show now some interferograms of Astigmatism (Z_2^{-2}), Defocus (Z_2^0), Coma (Z_3^1) and Spherical Aberration (Z_4^0) with an a RMS of $0.3\lambda(633nm)$ each.

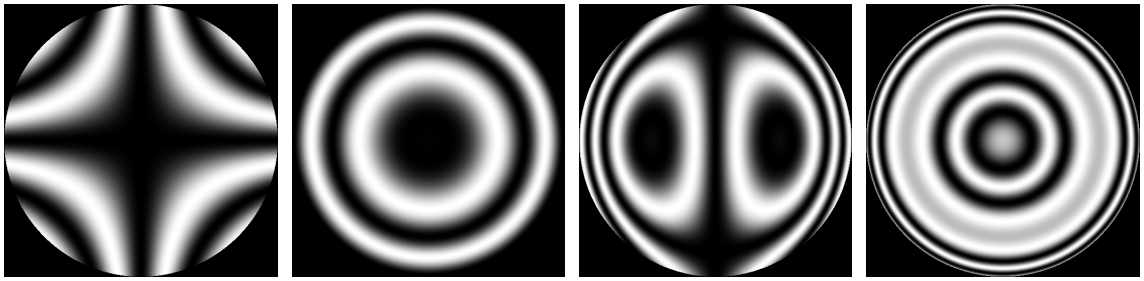

(a) Astigmatism **(b)** Defocus **(c)** Coma **(d)** Spherical Aberration

In the following the preferred way of representing a wavefront will be using interferograms assuming a wavelength of $633nm$.

3.1.2 Wavefront correctors

In general, a wavefront corrector device has the role to introduce an optical path difference in order to correct the aberrated wavefront or, alternatively to reproduce intentionally a particular wavefront shape.

The optical path difference (OPD) for a light ray traveling a distance d is:

$$\delta = \Delta(n \cdot d) \tag{3.3}$$

where n is the refraction index of the traveling medium, and the corresponding phase imparted by this OPD is:

$$\phi = \frac{2\pi}{\lambda}\delta \tag{3.4}$$

hence from 3.3 an instrument with the goal of shaping the wavefront, has two possible ways to operate:

- acting on the refraction index of the medium in which the light passes through
- acting on the distance d the light has to travel.

A group of devices using the first principle are Spatial Light Modulators (SLM). A SLM can usually vary both the intensity and the phase of the incoming beam and liquid crystals are often used to this purpose because of the advantage of a great resolution in the range of $1 \div 2$ millions dots, giving them a high degrees of freedom in the correction capabilities used to correct for high aberrations orders.

Devices using the second principle are deformable mirrors or lenses. While different kind of deformable mirrors exists (segmented, membrane, bimorph, etc...) there is, at this moment, only the Adaptive Optics laboratory (IFN CNR) in Padova that develop multi-actuators deformable lenses in which the deformation is made possible using piezoelectric actuators placed in the borders of the lens. A simple illustration of a deformable lens can be seen in figure 3.4

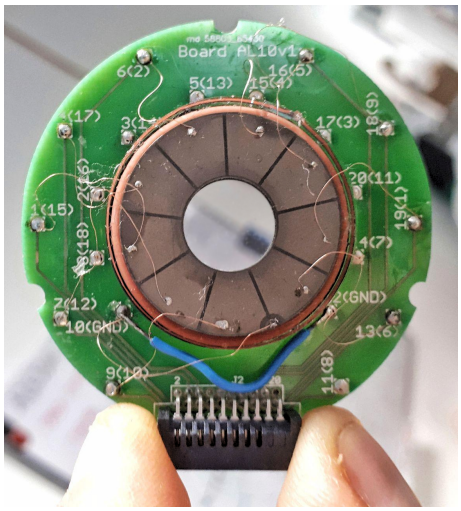

Figure 3.4.: A deformable lens developed by the Adaptive optics Lab IFN CNR in Padova

Once chosen the deformable device, one thing needed before beginning the correction is the calibration process, needed to have a map of the response of the deformable device seen from the wavefront sensor. One common way to do it is to associate every actuator of the deformable device to a vector of wavefront gradients.

The procedure is the following: Defining with m the number of actuators and with n the number of sampled points in the aperture pupil (this can be the number of lenses in a Shack-Hatman sensor), one can create a matrix with $2 \cdot n$ rows and m columns. In the j^{th} column are recorded the gradients (x component: rows $1 - n$ and y component rows $n+1 - 2n$) of the wavefront obtained when only the j^{th} actuator is poked.

We call this matrix the Influence Matrix (IM) or Poke Matrix, while the vector of gradients due to a single actuator poked is called the Influence Function.

In a matricial formalism one can write:

$$\overline{\varphi} = \overline{\overline{A}} \cdot \overline{c} \tag{3.5}$$

where $\overline{c}$ is a m-vector containing the coefficients that the actuators are poked and $\overline{\varphi}$ is the vector containing the x-component and the y-component of the wavefront gradient generated by this poke configuration.

The IM can be visualized in various ways and the one we will use in the following is the plot of the interferogram of the influence function of each actuator.

As an example, the influence function of the lens shown in figure 3.4 is shown in figure 3.5

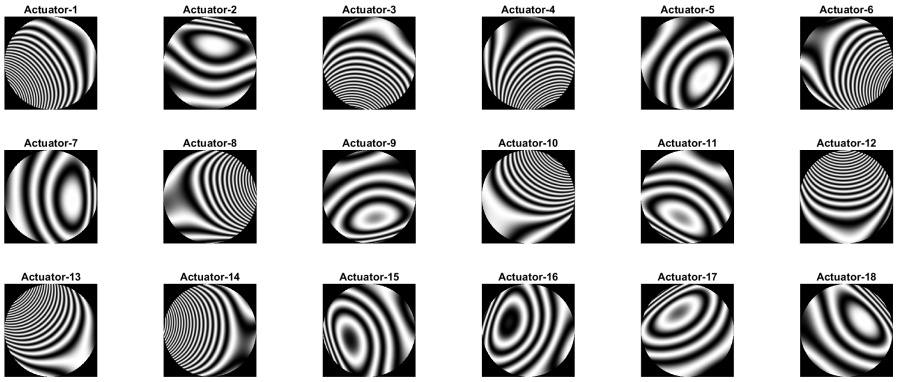

Figure 3.5.

3.1.3 Control Systems

The last element to make the adaptive optics system working is the control system. The aim of the correction stage is to shape the wavefront $\overline{\varphi}$ to a target one $\overline{\varphi_0}$ Once the wavefront is measured, the error $\overline{e} = \overline{\varphi} - \overline{\varphi_0}$ can be used to compute the poke coefficients to give to the deformable device.

To do so the inverse matrix of A needs to be computed. Usually though this matrix is not square and the inverse is given by the pseudo-inverse. We call this the control matrix C. So, the poke coefficients are given by:

$$\overline{c} = \overline{\overline{C}} \cdot \overline{e} \tag{3.6}$$

There are two possible control laws that can be used to correct:

- Open Loop
- Closed Loop

In the first case the wavefront sensor is placed before the deformable device. In this configuration the error is not dependent on the correction process because we are measuring only the incoming wavefront and we have no direct measure of the wavefront after the correction. For this reason the calibration is crucial because the effectiveness of the correction is highly dependent on this.

The latter case happens when the wavefront sensor is placed after the deformable device. In this case during the correction process we will see diminishing the error $\overline{e}$

and the poke coefficients must be added during the loop. This adds an instability to our control system, so the poke coefficients must be scaled by a factor k smaller than one (a value around 0.9 is usually used) to avoid oscillations. So the final poke coefficients are:

$$\overline{c} = k\overline{\overline{C}} \cdot \overline{e}$$

3.1.4 Sensorless Adaptive Optics

Is possible, when the aberrations are stationary and does not change over time, to correct for aberrations without the use of a sensor device. This kind of approach finds it's one of it's use in microscopy where aberrations are sample dependent thus are stationary. One of the main advantages of this approach is the fact that the system can be more compact and the integration of AO is almost seamless.

The founding principle of sensorless AO, first conceived in 1974[10] is the maximization of a metric (usually it is the image intensity squared, but every good metric can be used).

In this case, the AO element must be calibrated before. Then an algorithm spans over the singular modes of the deformable device. In practice the algorithm tries different configuration of $\overline{c}$ and the correction is done choosing the coefficients $\overline{c}$ that maximize the metric.

3.2 PUPIL SEGMENTATION

The pupil segmentation (PS)[11] is a very recent wavefront measurement technique.

As already said in the section Modern optics and Image Formation, if an object is placed near the lens, the lens forms in his focal point a (almost) Fourier transform of it (let aside a some phase factors accounting for pupil size and apodization). Moreover, every point of the back pupil of a lens, contribute for the formation of the image. In fact if we could place an iris in the back aperture pupil of the lens, the result in the image plane will be the same image, with a decreased resolution and intensity due to the smaller NA induced by the smaller aperture.

If we suppose the image is aberrated, this will means that the incoming wavefront is not flat. The founding idea of the pupil segmentation is to scan the wavefront placing an aperture in different positions of the back aperture pupil of the optical system and record an image for every aperture position.

If the aperture is sufficiently small (i.e. the highest not negligible wavefront spatial frequency variation is larger than the aperture diameter) we can consider the wavefront in each aperture only affected by local tip-tilt. This will therefore impact on the image formation as a shift. We can then measure the shift of each image using an appropriate algorithm. Then the procedure to reconstruct the wavefront is the same as the one described in the Wavefront Sensors subsection.

Part II.

Experimental setup and Results

4 OBJECTIVES CHARACTERIZATION AND SA MEASUREMENTS

The presence of spherical aberration, as already covered in chapter "Spherical Aberration in Microscopy", is one of the most common cause of image degradation in microscopy.

in fact, spherical aberration is one of the easiest aberration that can be reproduced in a microscope setup because it can arise from a refraction index mismatch as shown in section 2.2.1, and for this reason it is almost always present in the study of biological samples[1] where oil immersion objectives are often used. However even when water designed objectives are used in the study of biological samples, spherical aberration can arise because of the refractive index mismatch of different tissues or sub-cellular components in the optical path.

For this reason I built a setup aimed at the measurement and the correction of spherical aberration with different objectives and mismatch thicknesses using a Shack-Hartman WS and an adaptive lens developed by the Adaptive Optics Lab of the IFN CNR Institute of Padova. This kind of lens has already been used in the correction for aberrations in an Optical Coherence Tomography system for in vivo imaging of mouse retinal structures[13] and in a confocal microscope using a sensor-less algorithm [14].

Spherical Aberration has already been corrected using deformable mirrors, (DM) [15] where they were able increase the axial scanning range from $150\mu m$ to $600\mu m$ of a 40x/0.6NA objective used in a scanning multiphoton microscope using a deformable mirror with a genetic algorithm used for the correction, or using spatial lights modulators (SLM) [16] where a large amount of spherical aberration can be corrected and with a high resolution.

One of the main advantages to use a deformable lens instead of DM or SLM is the fact that it is a transmissive element and the optical path does not need to be folded. This can be a crucial advantage where a compact optical path must be used or when it is impossible to modify the optical path with mirrors. This in fact is often the case in microscopy where the optical setup is usually complex and the alteration of the optical path can be very difficult and often limited bu the microscope enclosure itself.

4.1 SETUP

The setup consist of a $670nm$ laser diode, followed by a $f = 100mm$ $\varnothing 1''$ collimation lens. The quality of the collimation was checked with a shear-plate interferometer. Then was placed the deformable lens module[2] and two relay lenses of $f = 150mm$ and $f = 250mm$

1 The refractive index of biological material is similar to that of water ($n \simeq 1.33$) and can span from $n \simeq 1.33$ to $n \simeq 1.48$

2 The deformable lens was composed of two separate modules in series. One is the one shown in figure 3.4 with 18 actuators, followed by a single actuator deformable lens specifically designed to correct for

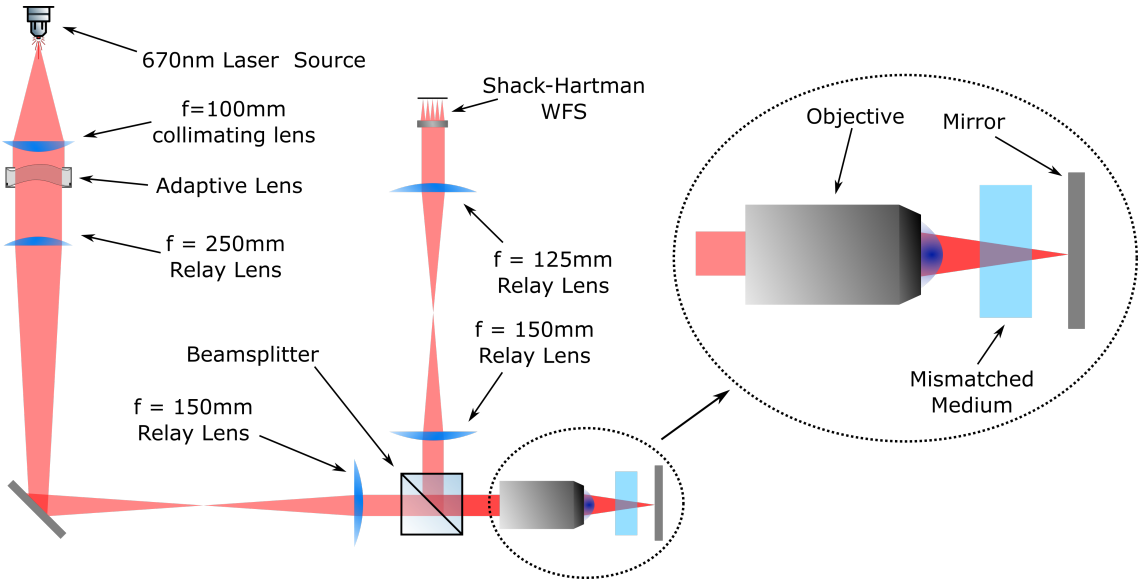

Figure 4.1.: Setup used for the characterization and correction of SA of in a objective

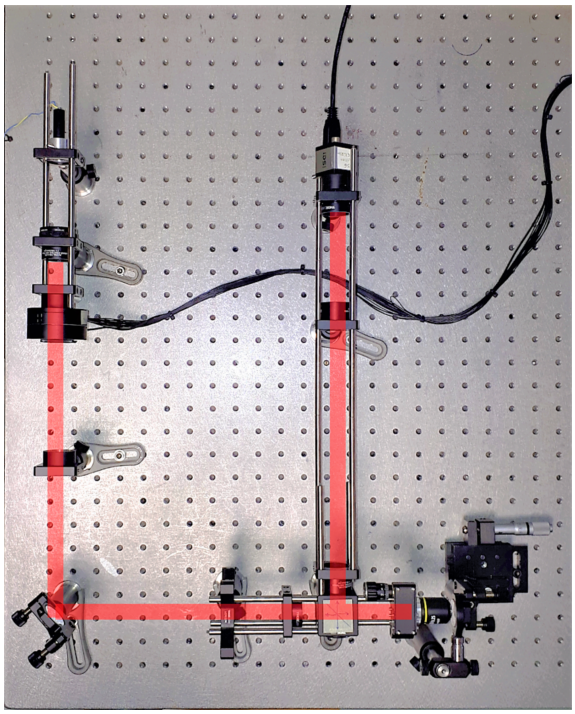

Figure 4.2.: Image of the Setup

in order to create the image of the pupil of the deformable lens in the back aperture pupil of the objective lens. Moreover this is necessary to match the deformable lens clear aperture (10mm) to the back aperture diameter of the objective used in order to be sure to use the whole dynamic range of the AL. In practice it is better to setup the relay lenses to create a little bigger image of the back aperture pupil of the objective lens to the AL plane. Likewise, the image of the AL clear aperture to the back aperture pupil

spherical aberration. The first module in fact can correct only up to $\simeq 0.2\lambda$ RMS of SA, while with the second module added, the system can correct for $\simeq 0.5\lambda$ RMS of SA.

of the lens (so the diameter of the light beam) will be smaller than the back aperture pupil diameter. In this way we are diminishing the NA of the objective lens in order to preserve the dynamic range of the lens.

Two single axis translator (coarse and fine) were then used to move the focus plane of the objective where a ∅1″ broadband mirror was placed.

Between the second relay lens and the objective I placed a 50 : 50 beamsplitter, oriented in a way that the reflected beam is again reflected to the wavefront sensor.

Two others relays lenses ($f = 150mm$ and $f = 125mm$) were used in order to create an image of the back aperture pupil of the objective (and of the adaptive lens pupil too) in the wavefront sensor plane.

In this way we have tree conjugated planes:

- the deformable lens plane
- the objective back aperture pupil plane
- the WFS plane.

4.2 THE METHOD

As already said, for every Objective used the relay lenses configuration was modified to match the Adaptive lens clear aperture diameter to the objective back aperture pupil diameter. This means that the initial aberration due only to the optical path without the objective and the AL needs to be measured every time we change the objective lens. This initial aberration was then subtracted from each of the following measures utilizing the same configuration in order to keep the measure free of the system aberration.

Every wavefront measured was taken averaging at least 400 measures and the error associated was obtained computing the square root of the mean variance.

It's easy in this configuration to produce spherical aberration just placing between the objective lens front element and it's focal plane a medium with a refractive index different from the design one of the objective. It must be noted that in this configuration the light passes two times in the mismatched medium because of the mirror. So the amount of SA measured is doubled respect to the one obtained in a single pass configuration.

I had to my disposal three objectives from an "Eurotek Bioline N300" commercial transmission microscope:

- NA = 0.25 AIR, 10x, 0.17/inf
- NA = 0.65 AIR, 40x, 0.17/inf
- NA = 1.25 OIL, 100x, 0.17/inf

The number near the numerical aperture is the magnification. The following, means that the objectives are already corrected for spherical aberration induced by a single $0.17mm$ coverslip and they form an image of the object at infinity.

To produce SA with air objectives I used glass of different thicknesses:

- 6mm, $n = 1.456$ fused silica
- 1mm, $n = 1.518$ microscope slide
- 0.17mm, $n = 1.518$ microscope coverslip

while for the oil objective, an air gap ($n = 1$) and polyvinyl acetate sheet ($n = 1.47$) was used.

All the refractive indexes are considered at $\lambda = 670nm$.

From section 2.2.1 emerges that the amount of SA depends linearly on the mismatch depth d and has a high non-linear dependence on the NA of the objective. This means that to produce the same amount of SA, with an higher NA objective we need to lower the mismatch thickness.

Before starting with the measurements, a calibration of the lens was made:

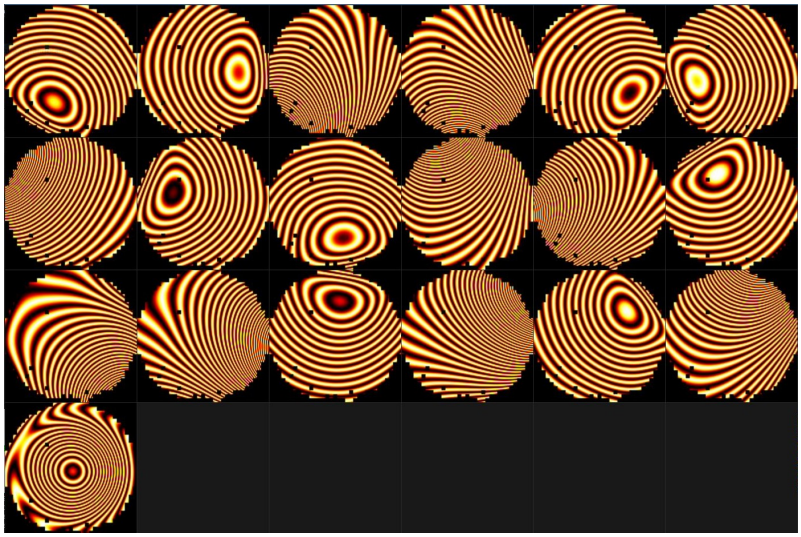

Figure 4.3.: Influence functions of the lens actuators

4.3 MEASUREMENT AND CORRECTION

For all measurements we will show the interferogram, the zernike coefficients and, only for the first measurement, the image seen from the Shack Hartman sensor.

4.3.1 NA = 0.25 AIR, 10x, 0.17/inf OBJECTIVE

The aberration due only to the optical path without the objective and the DL can be seen in figure 4.5. With an RMS wavefront error of $(0.067 \pm 0.004)\lambda$ we are diffraction limited in accordance with the Maréchal criterion. This initial aberration will be subtracted to the following measures.

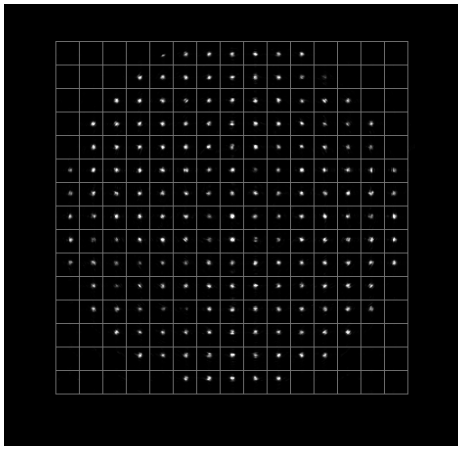

Figure 4.4.: Shack Hartman sensor image of the path aberration of the setup used without the NA = 0.25 Objective and the AL

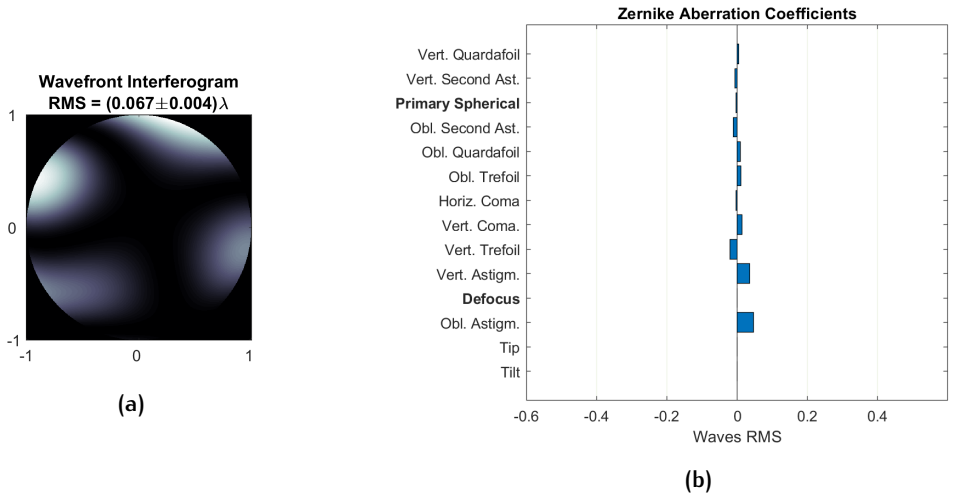

Figure 4.5.: Path Aberration of the setup used without the NA = 0.25 Objective and the AL

We can now add the objective lens.
In figure 4.6 the measure taken with the objective and with no AL in the optical path and a 0.17mm coverslip can be seen. We can see that the wavefront is not diffraction limited anymore, this means that the objective itself introduces some, although not large, aberrations.

Introducing then a 6mm thick fused silica glass between the objective lens and the mirror in the focal plane, we can see in figure 4.7 that, as expected, the main source of aberration is Spherical aberration with $SA = (0.15 \pm 0.04)\lambda$ and we are far from being diffraction limited.

Introducing the adaptive lens and closing the correction loop, we can measure the corrected wavefront.

After the correction, shown in figure 4.8, the wavefront RMS is again under 0.07λ and can be considered diffraction limited. In particular we can see that the system can correct successfully for spherical aberration letting a residual $(0.0482 \pm 0.0002)\lambda$ RMS of SA.

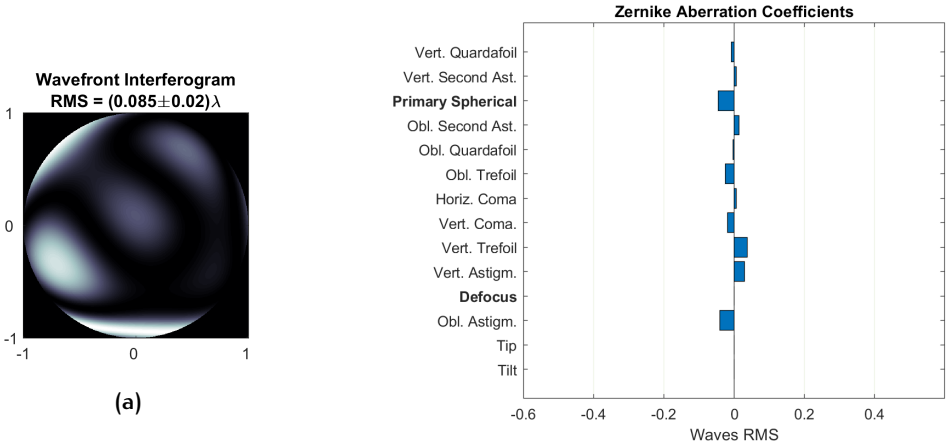

Figure 4.6.: Path Aberration of the setup used with the NA = 0.25 Objective and no AL

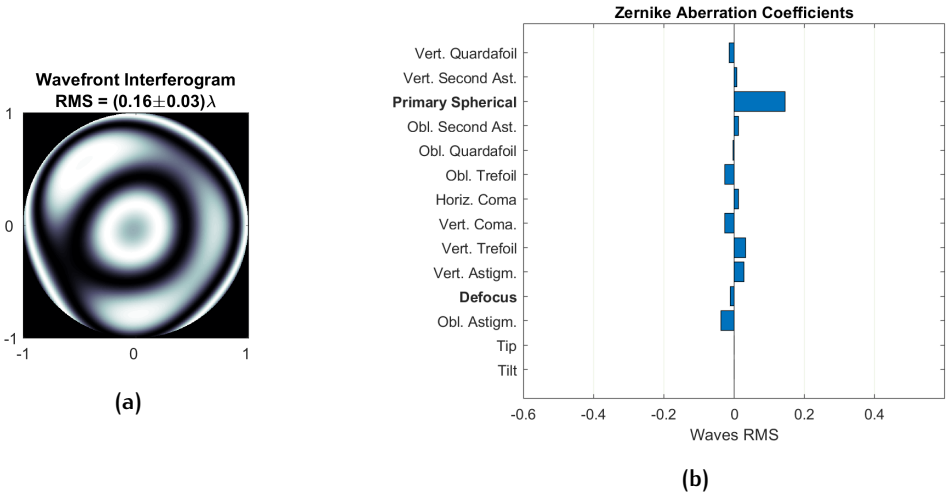

Figure 4.7.: Path Aberration of the setup used with the NA = 0.25 Objective and a mismatch of d = 6mm silica glass and no AL

4.3.2 NA = 0.65 AIR, 40x, 0.17/inf OBJECTIVE

Repeating the same procedure, I changed the objective to the "NA = 0.65 AIR, 40x, 0.17/inf". The measure without the objective shows only a little bit of astigmatism, even so the system can be considered diffraction limited.

Mounting the objectives and the 0.17mm coverslip lead to an aberration shown in figure 4.11. The objectives introduces some, although not much, aberrations. In particular SA with $(-0.074 \pm 0.001)\lambda$ and astigmatism with $(-0.050 \pm 0.002)\lambda$, and cannot be considered diffraction limited anymore.

We can now add another 0.17mm coverslip [3] and measure the wavefront again.

3 We cannot use the 6mm silica glass because the magnitude of SA depends very strongly with the NA of the objective, and a 6mm silica glass produce a SA that cannot be measured

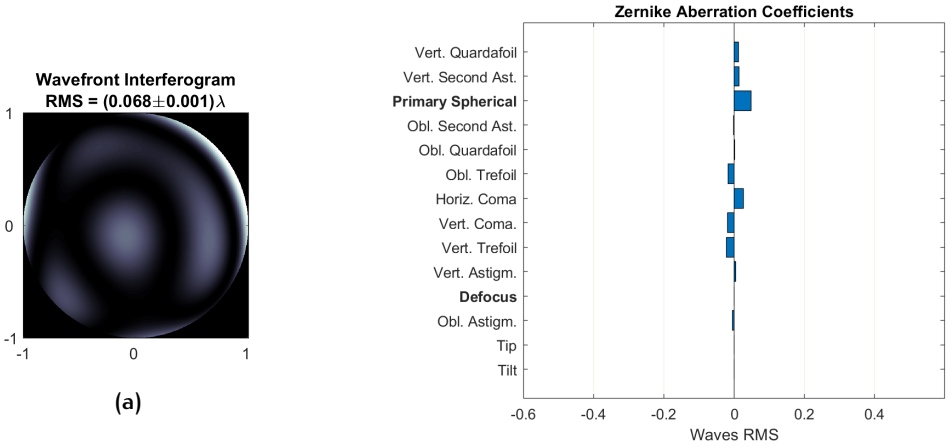

Figure 4.8.: Path Aberration of the setup used with the NA = 0.25 Objective and a mismatch of d = 6mm silica glass after AL correction

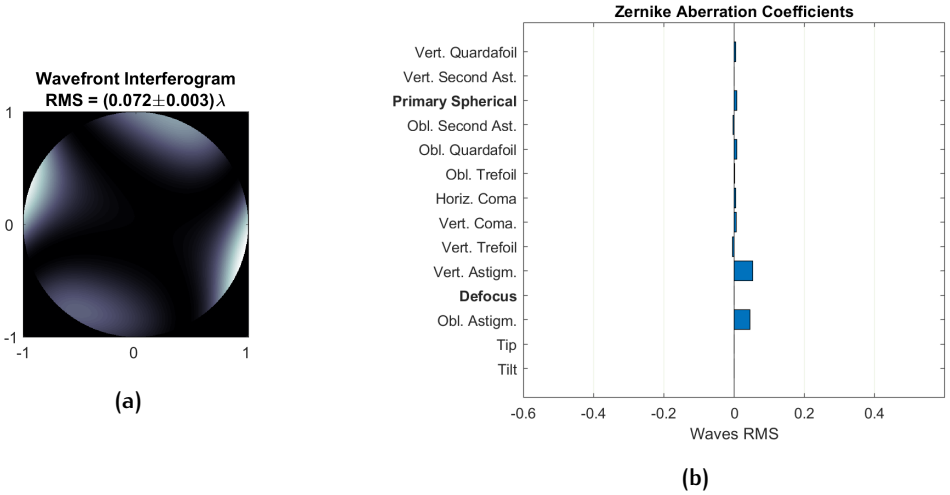

Figure 4.9.: Path Aberration of the setup used without the NA = 0.65 Objective and the AL

The SA in now evident to be the main source of aberration with an RMS of with $(0.374 \pm 0.001)\lambda$. So the coverslip introduces a SA of $(0.448 \pm 0.02)\lambda$.

It is now possible to introduce the AL and close the correction loop to correct the aberrations.

The results of figure 4.12 shows a that the AL were able again to recover for the aberrations of the mismatch.

4.3.3 NA = 1.25 OIL, 100x, 0.17/inf OBJECTIVE

Changing to the NA = 1.25 OIL, 100x, 0.17/inf objective setup, we can see in figure 4.13. As usual just a little bit of astigmatism is present.

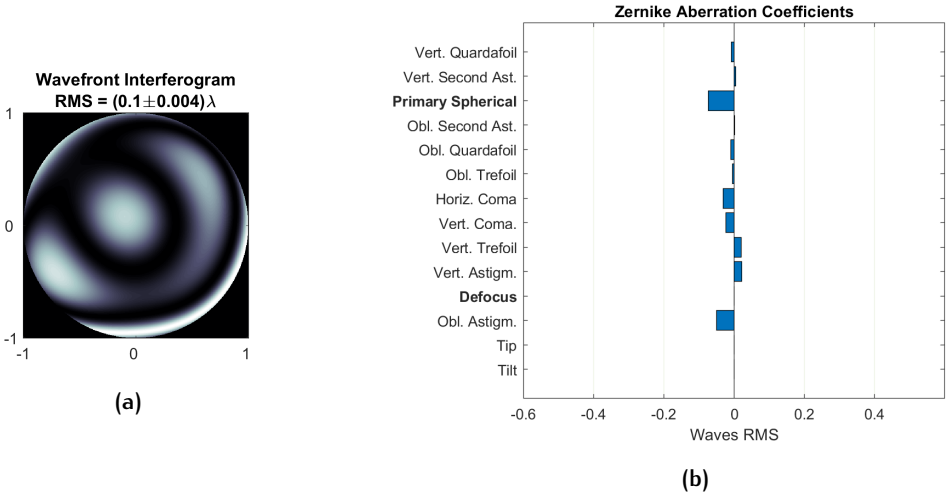

Figure 4.10.: Path Aberration of the setup used with the $NA = 0.65$ Objective and no AL

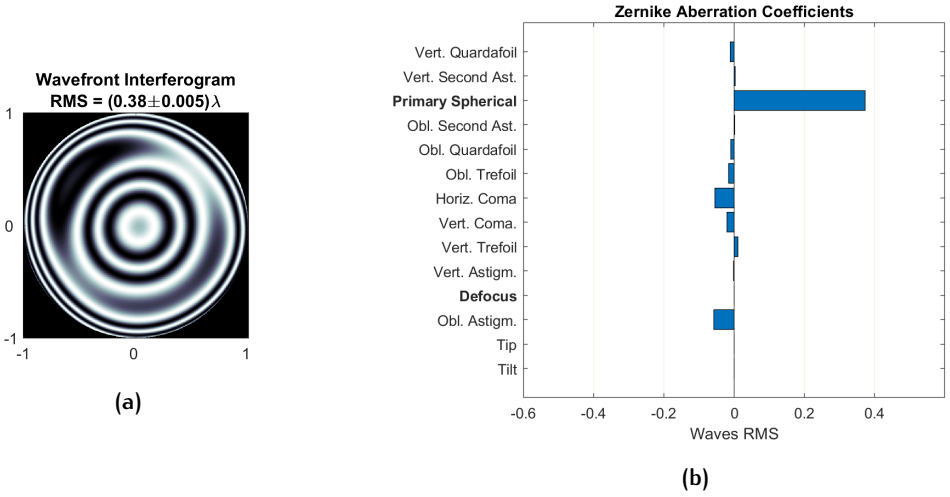

Figure 4.11.: Path Aberration of the setup used with the $NA = 0.65$ Objective and a mismatch of $0.17mm$ BK7 glass

Being an oil objective, to work properly microscope oil ($n = 1.518$) must be used between the objective front element and the mirror.

Inserting now the objective with oil, we can see in figure 4.14 that there is already present a little bit of SA ($(0.067 \pm 0.001)\lambda$), so the objective is not perfectly corrected for it and the system is not diffraction limited.

Adding a $5\mu m$ thick acetate sheet into the focusing path lead to a more flat wavefront (figure 4.15) with a reduced SA, but in this way we cannot produce a significant amount of SA.

I tried then to measure the wavefront removing the microscope oil. The amount of SA in now too big to be measured as can be seen in figure 4.15b

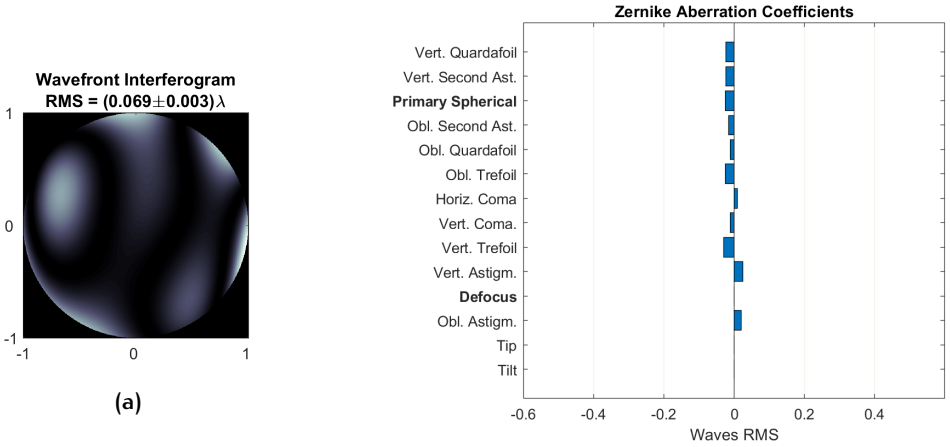

Figure 4.12.: Path Aberration of the setup used with the NA = 0.65 Objective and a mismatch of d = 0.17mm BK7 glass after AL correction

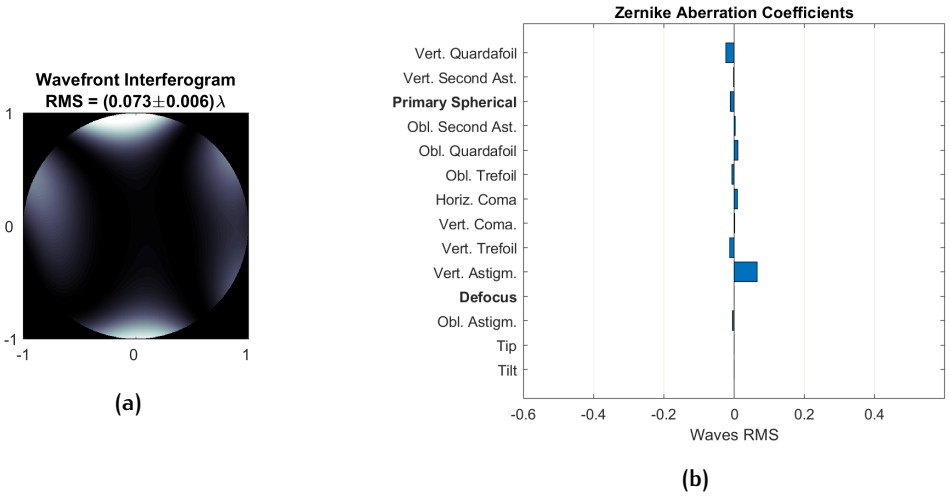

Figure 4.13.: Path Aberration of the setup used without the NA = 1.25 Objective and the AL

4.4 DISCUSSION OF THE RESULTS

This simple setup test was built in order to utilize three different objectives out of their working configuration to simulate a typical condition in biological microscopy where spherical aberration is one of the main source of image quality deterioration.

The most important result is that it is possible to correct for this aberration with a deformable lens, instead of the always used DM or SLM devices recovering, diffraction limited results.

This test showed a correction capability of the lens of $\simeq 0.5\lambda$ RMS of Spherical aberration.

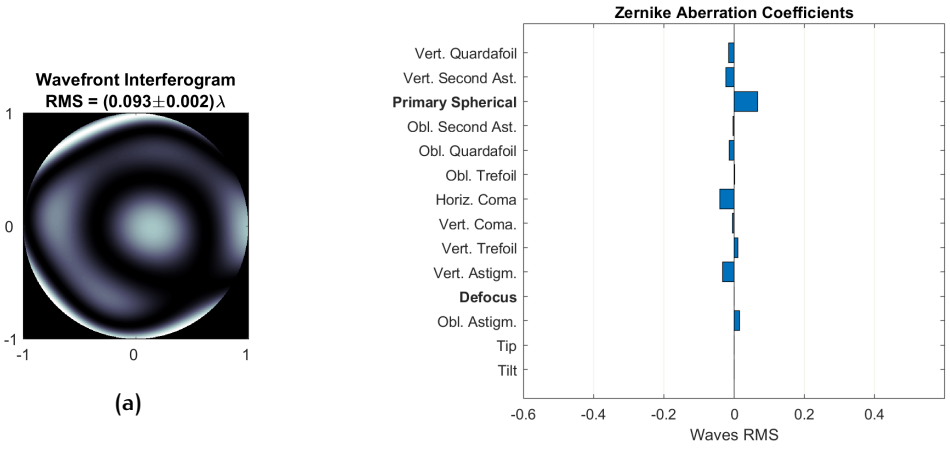

Figure 4.14.: Path Aberration of the setup used with the NA = 1.25 Objective and oil (n = 1.518) but no AL

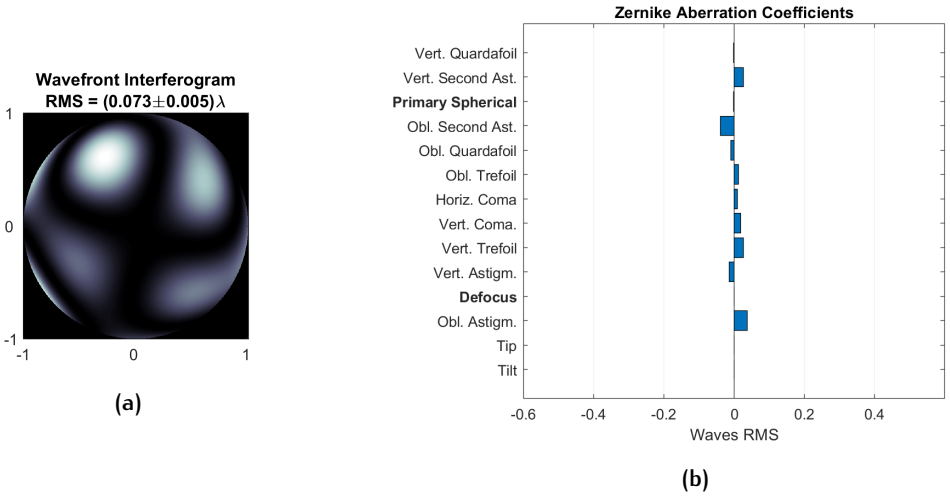

Figure 4.15.: Path Aberration of the setup used with the NA = 1.25 Objective, oil (n = 1.518), and a 5µm thick acetate sheet, but no AL

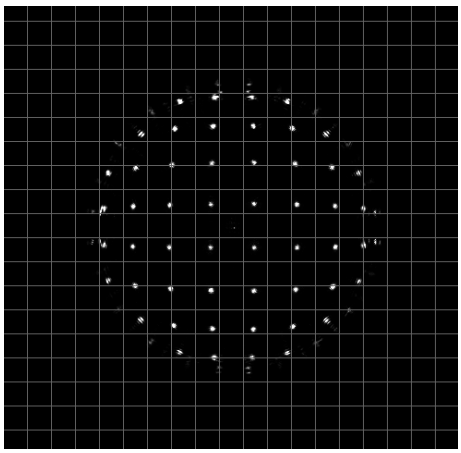

Figure 4.16.: Shack Hartman sensor image of the aberration obtained with the NA = 1.25 oil objective used without the microscope oil

5 PUPIL SEGMENTATION IN A BRIGHT FIELD MICROSCOPE

The founding principle of the pupil segmentation technique [11] is that we can divide the back pupil of the objective in many sub-apertures; each sub-aperture creates an image of the sample on the scientific camera (with a reduced resolution given by the smaller aperture, hence lower NA). If the outcoming wavefront is aberrated, each image created by the sub-apertures is shifted respect to the others. From this shift we can reconstruct the gradients of the wavefront and thus the wavefront itself. Is not difficult to see that this method cannot measure and correct for tip and tilt by construction. In fact to compute the relative shift, we need to chose a reference image. This is because tip/tilt aberration is common to all points of the aperture pupil, and it cancels out when computing the relative shift of two images originated by two different point of the aperture pupil. So the PS technique is blind to tip-tilt aberration. However this is not a problem, because tip/tilt are not a real aberration because represents just a shift of the image and (in microscopy) does not affect the image quality.

A first study with simulations and some preliminary experimental results were already conduced in a degree thesis [12]. So we decided to apply this technique to a real microscope setup for correcting an induced spherical aberration.

5.1 SIMULATION OF THE MEASUREMENT PROCESS

In section Pupil Segmentation, we saw the main concepts below the Pupil Segmentation. In particular, one of the key points is the fact that every point in the back aperture pupil of an objective concur to the formation of the final image, thus with just a portion of the back aperture pupil of a lens, we can see the whole image with a lower resolution due to the diminished NA. Moreover in section Abbe Theory of Image Formation we saw that in the image plane the image formed is the convolution of the PSF of the system with the original image and that the system PSF in the focal plane is a quasi Fourier transform of the pupil function.

Now, let's consider the figure 5.1. On the left side, the object is shown[1].

I then generated some random aberrations, assuming that these aberrations are coming from the imaging system and/or from the sample itself. In the central-left column from top to bottom we can see the interferogram of the aberrated wavefront, the PSF of the system due to this aberration and then the image that is the convolution of the object with the PSF of the system. We can clearly see that the image quality is very deteriorated.

1 in this simulation the object are some pollen, but it is just for a demonstrative purpose

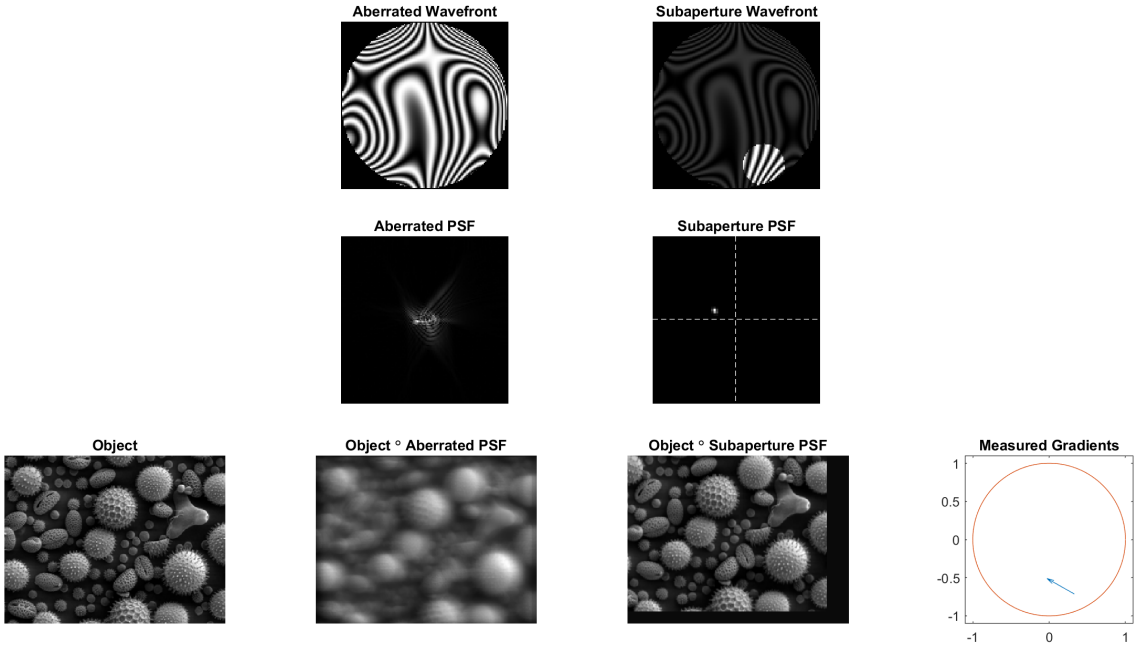

Figure 5.1.: Simulation of a Pupil Segmentation measurement process

If now we block all light passing through the aperture pupil, let aside a small opening (this situation is represented in the "Subaperture Wavefront" image), the system has a new PSF due only to this smaller aperture. We can see in "Subaperture PSF" that this PSF is not centered, thus the image that we see (the convolution between the object and the Subaperture PSF) is shifted.

Recording all images (thus the shifts) obtained from all the 18 subapertures we can compute the gradients of the wavefront using formula 3.1:

$$\nabla W|_{(x_i,y_i)} = \frac{\Delta_i}{f \cdot \lambda} \tag{5.1}$$

where f is the focal length of the tube lens and Δ_i are the images shits.

In reality, to compute the shifts, we do not have to our disposal the non aberrated image, so we need to chose a reference image between the 18 images taken during the process. This will inevitably add some tip/tilt components that must be set to 0 in the process. Because of this, this method is blind to $tip - tilt$.

Let's denote with $\overline{\varphi}$ the 36-rows vector containing the 18 $x-$components followed by the 18 $y-$components of ∇W. If we want to correct for this aberration we need to give the right instructions to our correction element (i.e. the deformable lens). Recalling that, the influence matrix ($\overline{\overline{A}}$) of the lens, obtained during the calibration process of the lens, is a 36X19 matrix, containing in each column the gradients (always $x-$components followed by the $y-$components) that a single pocked actuator will produce, and remembering that $\overline{c}$ is the vector containing the poke coefficients of the lens (i.e. the actuators voltages of the lens); of course the product $\overline{\varphi'} = \overline{\overline{A}} \cdot \overline{c}$ will produce a wavefront with gradients $\overline{\varphi'}$.

Conversely, in our case we know the wavefront gradients and we want to know which actuators must be pocked in order to produce a gradient opposed to the measured one (in this way the lens will produce an opposite aberration and the net outcome will be, in ideal conditions, a non-aberrated wavefront).

This problem can be solved with a simple matrix calculation. Denoting with $\overline{\overline{C}}$ the pseudo-inverse matrix of $\overline{\overline{A}}$ (called control matrix), $\overline{c}$ is given by:

$$\overline{c} = -\overline{\overline{C}} \cdot \overline{\varphi} \tag{5.2}$$

5.2 THE PUPIL SEGMENTATION MODULE

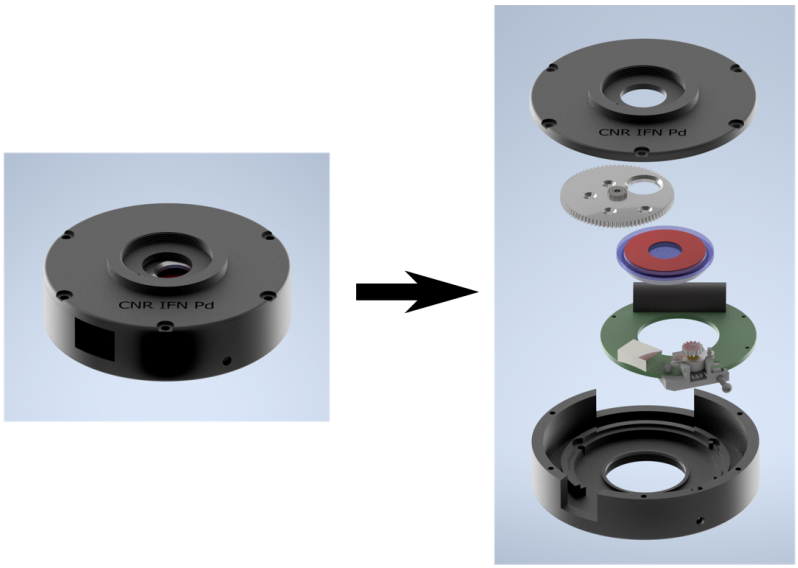

Figure 5.2.: 3D rendering of the newly designed pupil segmentation module.

The Pupil Segmentation module is custom built (figure 5.2). It has a 3D printed case where the AL, the rotating wheel with the subapertures and the stepper motor are located.

The case has a threaded hole in order to mount the module in a standard ThorLabs mount.

The wheel is aluminum made CNC milled, with 4 holes with a diameter of 2.5mm positioned at different radial distances and the main aperture with a diameter of 10mm, mounted on a bearing and free to rotate on it's axis. The rotation is controlled using a stepper motor.

To drive the lens and the wheel I wrote a Matlab UI.

Theoretically, the radial segmentation is limited by the number of holes in the wheel and the angular segmentation is limited by the smaller step achievable by the stepper motor (3°).

We choose use a total of 18 subapertures.

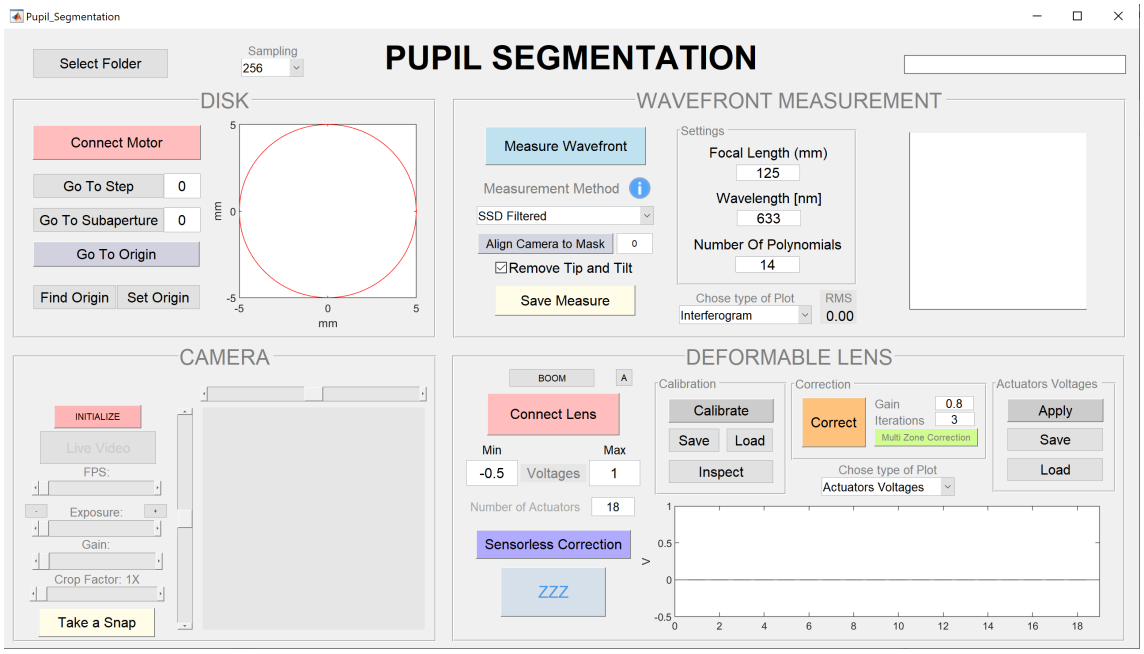

Figure 5.3.: Newly Designed Matlab GUI

Figure 5.4.: Matlab GUI used to drive the Pupil Segmentation module.

This choice is a compromise between sampling density and illumination loss. In fact, in order to measure correctly up to the 4^{th} order of Zernike polynomials (in total $n = 14$ polynomials) it is necessary to sample with at least with $2n + 1 = 29$ points. This will lead to smaller holes and a further loss of light.

This limitation though can be overcome by an iteration in the correction stage. To support this thesis I made some simulations shown in the next section.

5.3 ITERATION OF THE MEASUREMENTS

In this section, I will show how an iterative measurement process can overcome the under-sampling problem stated above.

In this simulation a random aberration is generated using all Zernike polynomials till the 14^{th} polynomial.

The wavefront generated by this aberration is then evaluated in the position of the 18 subapertures and from each of this sub-wavefront the PSF in the focal plane is computed. From the position of the peak of each PSF the wavefront is reconstructed, and the residual wavefront (the reconstructed wavefront subtracted to the original one) is computed. Then I made an iteration of this process, where the residual wavefront becomes the original one.

The results of the simulation can bee seen in figure 5.5 and figure 5.6

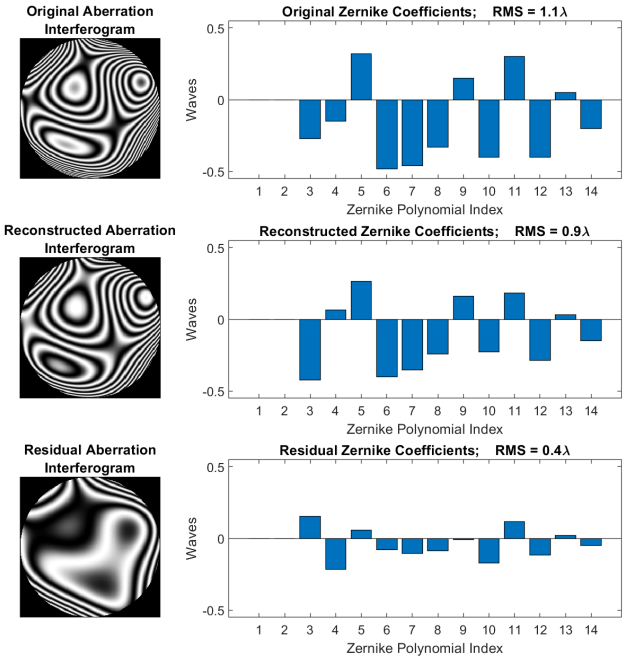

Figure 5.5.: First iteration of a simulated aberration and it's reconstruction using the 18 aperture configuration of the pupil segmentation module

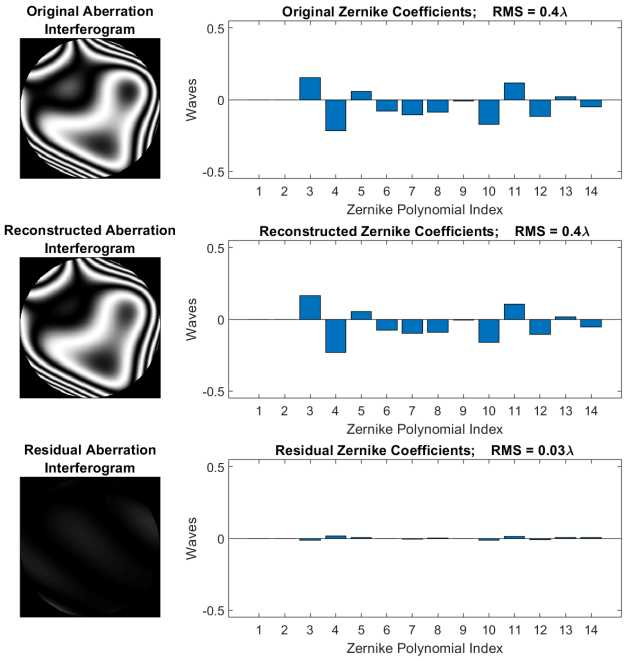

Figure 5.6.: Second iteration, in which the previous residual aberration becomes the original one.

It is evident that, although the system cannot measure the wavefront perfectly, a control system that uses an iterative process can overcome this limitation achieving a corrected wavefront.

This has been kept into consideration in the writing of the code for the correction process where at least three iterations are imposed.

5.4 SETUP

In order to mount the PS module to a microscope, we modified an existing bright field microscope removing the eyepiece section and we made an adapter to accommodate the ThorLabs mounting cage.

Figure 5.7.: Picture of the modified BF microscope

The setup we used is shown in Figure.5.8. In particular we used the $40x, NA = 0.65, 0.17/\text{inf}$ objective, followed by a relay of lenses to imagine the back aperture pupil of the objective to the pupil segmentation module.

A $125mm$ tube lens then form an image in a commercially available HD camera. Before the camera a band pass filter ($\simeq 450nm$) is placed to avoid possible chromatic effects.

The final magnification of the microscope into the camera image plane is approximately 20x.

5.5 RESULTS

To tested the setup I used an USAF target and some biological samples. To induce aberrations, as done in the previous chapter, we introduced (in addition to the one already

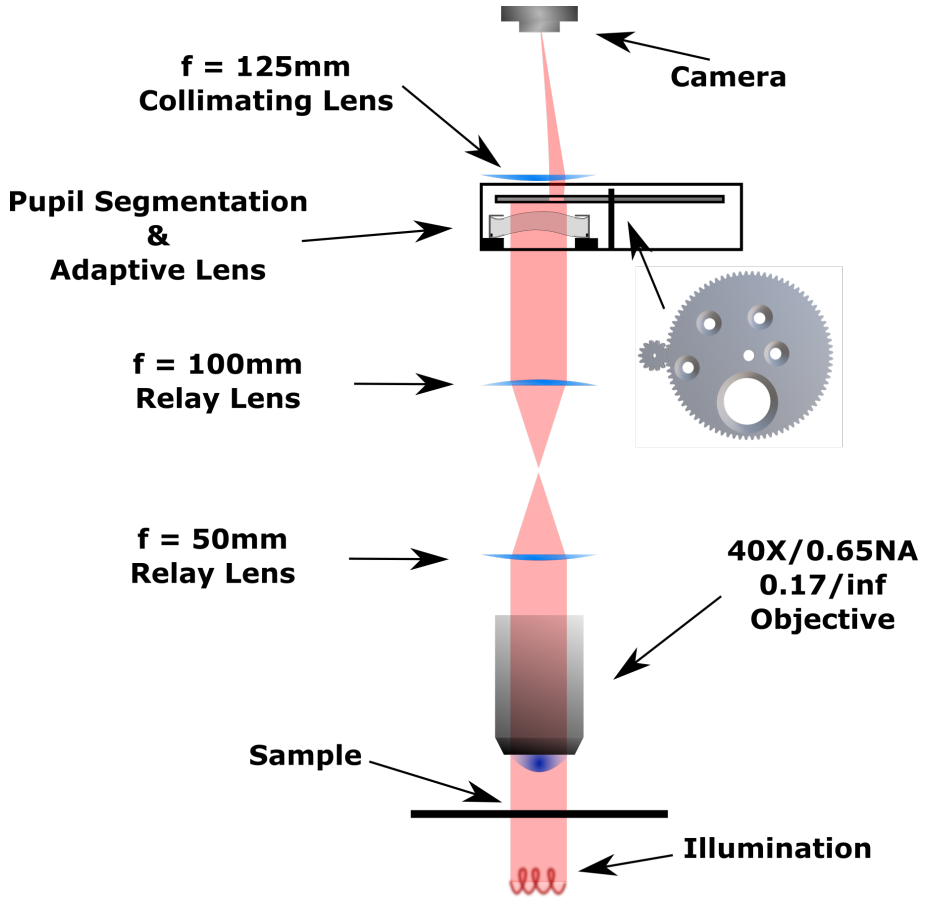

Figure 5.8.: Setup of the pupil segmentation module in a Bright Field microscope

present) one 0.17mm between the objective and the sample in order to reproduce aberration. Before the measurements, I gave the poke coefficients (obtained in the previous chapter) necessary to correct for the objective aberrations.

5.5.1 USAF target

The sample is a USAF target, a microscopic optical resolution test device composed of stripes of different dimensions orientated in vertical and horizontal directions. This chart is a standard one in microscopy when we want to test the optical resolution of a system. I chose to focus on the group 7 and element $1-2$ with a max line height of $3.48\mu m$.

After applying the corrections to the lens, I made a measurement of the aberrations (figure 5.10). As we can see the objective is now well corrected and diffraction limited.

Introducing a single 0.17mm coverslip (figure 5.12) we can see a big deterioration in image quality induced primarily by spherical aberration and coma.

After a 3 iteration correction (figure 5.14) we can see that the system is able to restore a diffraction limited image with an RMS $(0.04 \pm 0.01)\lambda$.

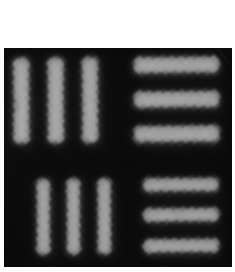

(a) Image

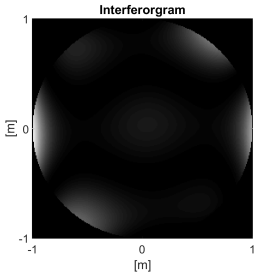

(b) Interferogram

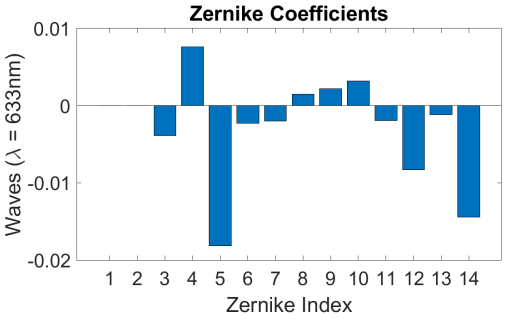

(c) Zernike Polynomials

Figure 5.10.: USAF TARGET corrected for the objective aberrations
RMS = $(0.03 \pm 0.01)\lambda$

(a) Image

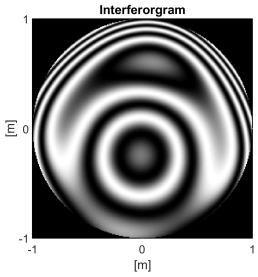

(b) Interferogram

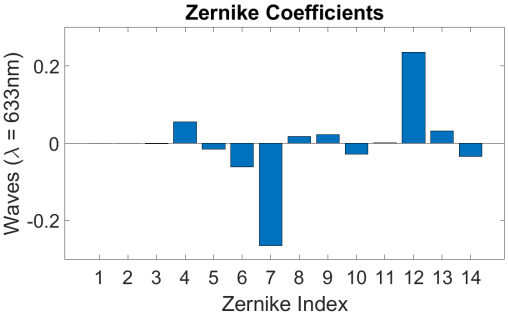

(c) Zernike Polynomials

Figure 5.12.: USAF TARGET with aberration induced by a 0.17mm coverslip
RMS = $(0.37 \pm 0.03)\lambda$

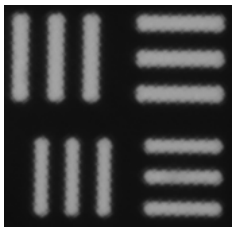

(a) Image

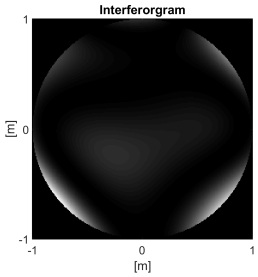

(b) Interferogram

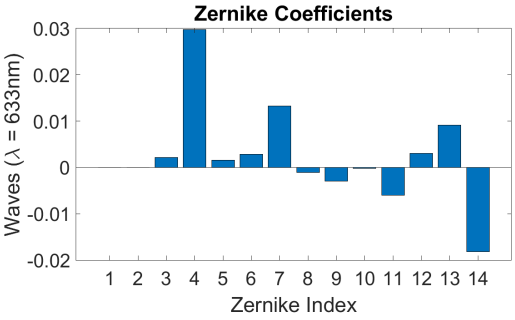

(c) Zernike Polynomials

Figure 5.14.: USAF TARGET corrected for the objective aberrations
RMS = $(0.04 \pm 0.01)\lambda$

Of course we need to remember anyway that all the measurement are affected by an under-sampling error. This means that coma-aberration in figure 5.12 might almost be non-existent (as we would expect from the measures of the previous chapter).

5.5.2 Corn Stem Sample

Changing the sample, I made the same measurements with a Corn Stem sample, available in our laboratory.

Starting with the image taken with the system corrected for the objective aberrations (figure 5.16) we can see that, as before, our system is diffraction limited.

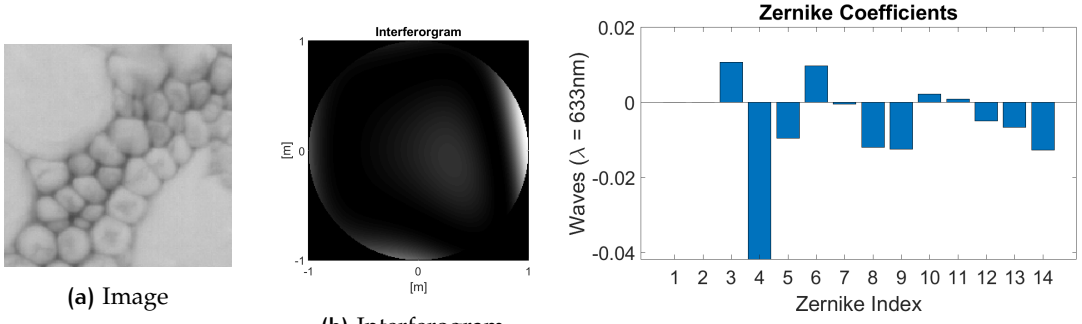

(a) Image

(b) Interferogram

(c) Zernike Polynomials

Figure 5.16.: Corn Stem sample corrected by the PS module
RMS = $(0.05 \pm 0.01)\lambda$

Introducing a single 0.17mm coverslip (figure 5.18) we can see again a deterioration in image quality induced primarily by spherical aberration and coma.

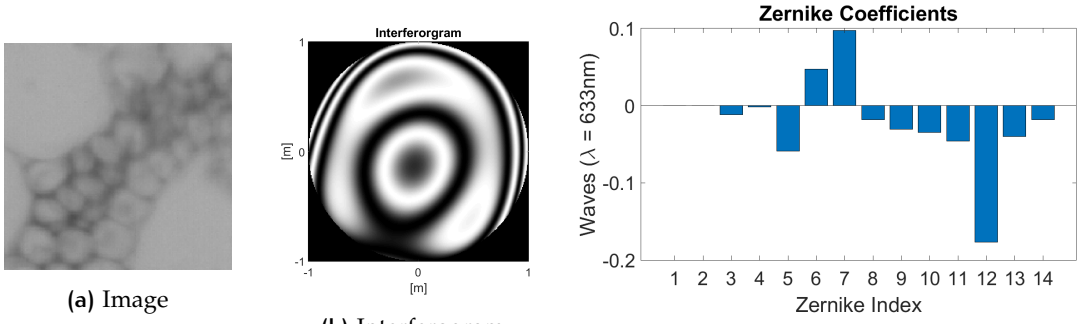

(a) Image

(b) Interferogram

(c) Zernike Polynomials

Figure 5.18.: Corn Stem sample with aberration induced by a 0.17mm coverslip
RMS = $(0.23 \pm 0.02)\lambda$

After a 3 iteration correction (figure 5.20) we can see that the system is able to restore a diffraction limited image with an RMS $(0.03 \pm 0.01)\lambda$.

5.5.3 Multi-Zone Correction

Up until now we chose to correct for aberration only in a small portion of the objective field of view; but it is often the case that we need to deal with an optical system (or a sample) with a non constant aberrations throughout the field of view. Usually the portion of the image that share a very similar aberration is called the isoplanatic patch.

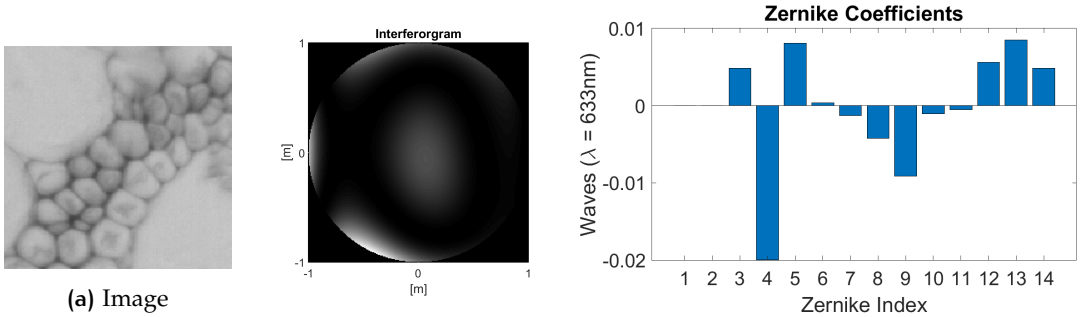

(a) Image

(b) Interferogram

(c) Zernike Polynomials

Figure 5.20.: Corn Stem sample corrected by the PS module
RMS = $(0.03 \pm 0.01)\lambda$

Obviously, because of this reason, the corrections we did in the previous sections are only local. So, with samples with an isoplanatic patch smaller than the field of view, to correct for aberrations the whole image we need to divide it into small sections, correct each section independently and then stitch together the corrected images.

To do so I chose a Dicotyledon sample, with a non-homogeneous depth. This can be clearly seen in figure 5.21. Is mandatory to say that this image is obtained with no AL in the optical path. In this way we can compare directly the results compared with and without the pupil segmentation module. for this reason, no measurement of the wavefront has been possible for this image.

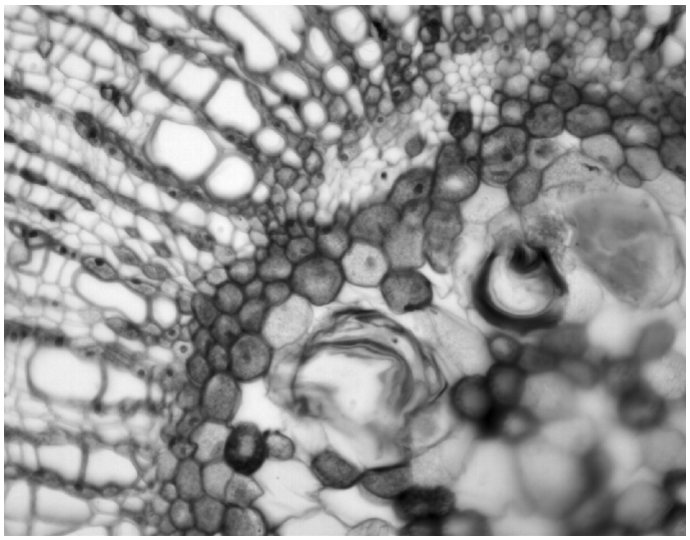

Figure 5.21.: Full field of view of a Dicotyledon sample. The non homogeneous depth is evident from the out of focus areas.

After reinserting back the PS module, I divided the field of view in 5x7 = 49 sections and I performed a correction for each o them. The results obtained stitching this images can me seen in figure:5.22 The choice of the division of the frame depends on the dimension of the isoplanatic patch and it has proved that a 5 by 7 division is enough.

In figure 5.23a from the interferograms of each zone, we can see that the correction was effective to restore a diffraction limited resolution almost everywhere with the exception

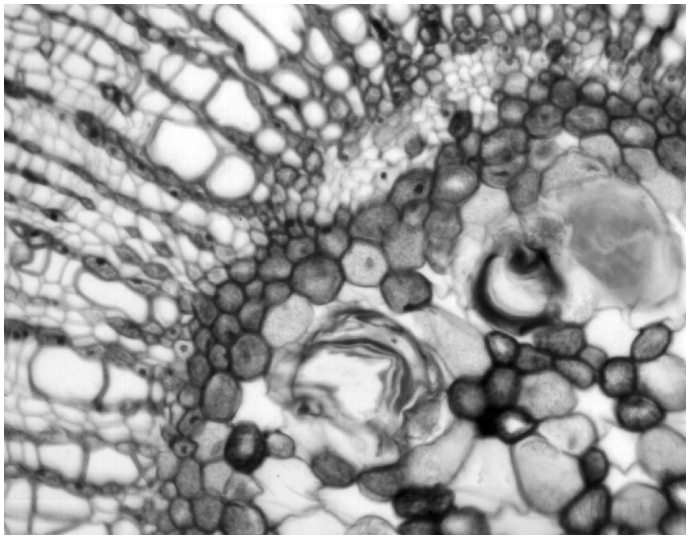

Figure 5.22.: Full field of view of a Dicotyledon sample. The non homogeneous depth is evident from the out of focus areas.

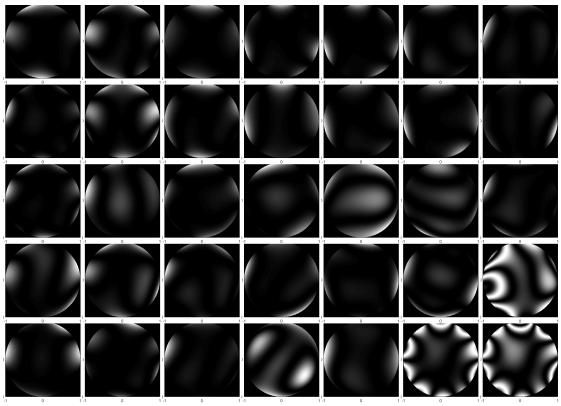

(a) Interferograms of the corrected sections of the image.

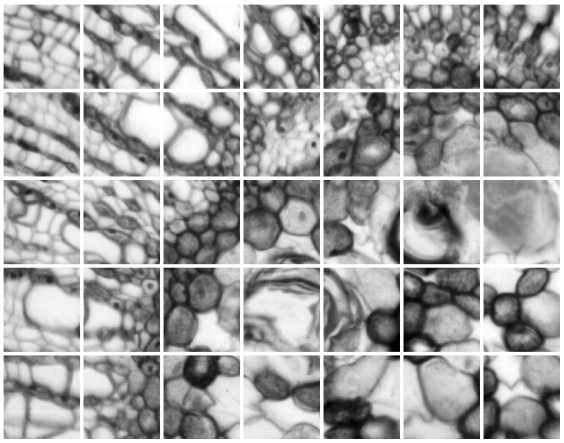

(b) Single images of the 49 sections.

of some regions where the initial aberration was too high to be corrected from the lens. In this regions the initial defocus was greater than 1λ RMS and the lens used all it's dynamic. Nevertheless the system was able to lower the aberration with a maximum residual of 0.17λ RMS.

5.6 DISCUSSION OF THE RESULTS

In conclusion we proved that is possible to use an adaptive lens in conjunction with a pupil segmentation wavefront measurement system in a bright field microscope with extended samples to correct for aberrations restoring diffraction limited images.

I tested this system both with an USAF resolution target and some biological samples.

The correction process takes less than a minute, and for this reason is better suited than sensorless algorithms in situation where the prolonged exposition to light can cause

photo-bleaching in the sample. Moreover this system can be very compact compared to other adaptive optics apparatus that uses deformable mirrors, so is more suitable to be integrated in existing microscopes.

Finally I showed that, dividing the FOW into sub-regions is possible to obtain a wide field correction stitching the individually corrected regions under the diffraction limit threshold almost everywhere.

6 PUPIL SEGMENTATION IN A LIGHT SHEET MICROSCOPE

After successfully correcting for aberrations in a Bright field microscope, the next step is to apply the pupil segmentation module to an existing microscope widely used to inspect biological samples.

At present day, one of the most used techniques is light sheet fluorescence microscopy (LSFM), also called single plane illumination microscopy (SPIM)[9].

A typical SPIM fluorescent setup consist of an illumination beam focused into the sample through a cylindrical lens. In this way only a single plane of the sample is illuminated. The detection is then decoupled to the illumination path with an objective with the optical axis orthogonal to the light sheet formed by the cylindrical lens. A schematic representation can be seen in figure 6.1.

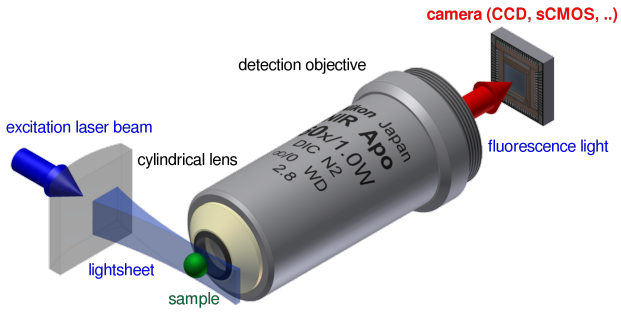

Figure 6.1.: A typical SPIM setup

Given the fact that we are detecting fluorescent light, a band pass or a long pass filter tuned for the fluorescence wavelength is usually placed in the detection light in order to exclude the light coming from the illumination path.

Thanks to a collaboration with the physics department of "Politecnico di Milano" we were able to access to a custom built light sheet microscope in order to mount the pupil segmentation module in the detection path.

As already said in Chapter 3, the position of the wavefront sensor and of the deformable lens, must be a conjugated plane of the back aperture pupil (BAP) of the objective lens. So in general there are two possible solutions:

- use a relay of lenses to form a conjugated plane of the BAP in a different position
- place the deformable lens exactly in the BAP of the objective.

While in the bright field configuration, described in chapter 5, I followed the first approach, in this case was possible to place the deformable lens (in conjunction with the

pupil segmentation module) immediately after the objective lens so the latter approach was feasible.

6.1 SETUP

The setup is the same described in [17] with the only differences consisting in a Nikon 10x air objective and the pupil segmentation module placed immediately after the objective lens.

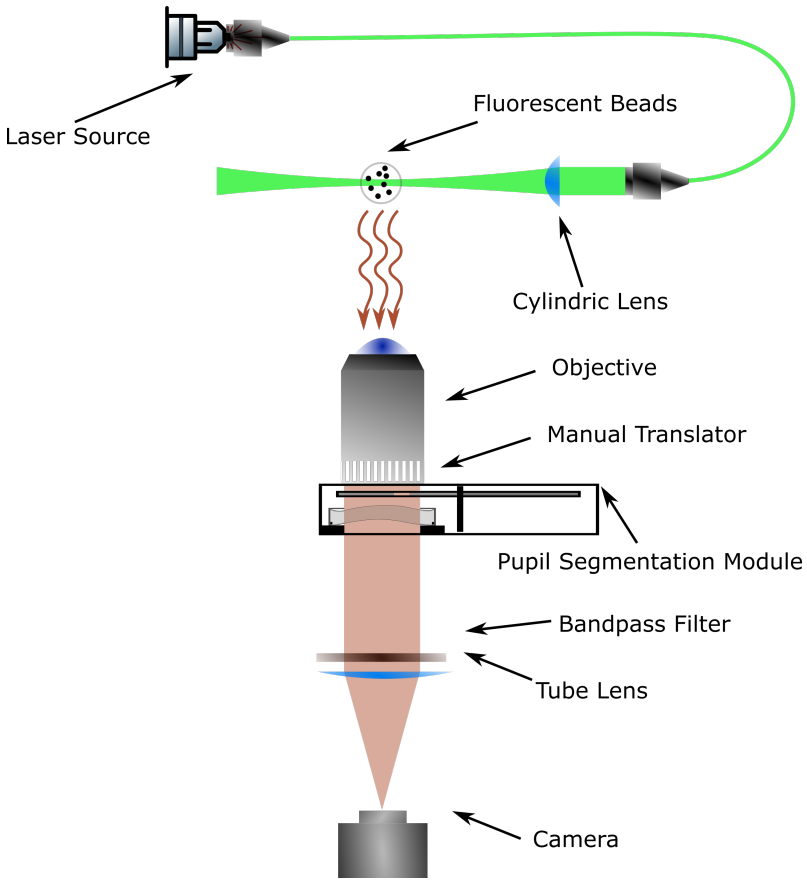

Figure 6.2.: The experimental setup

For the illumination path, a 532nm diode laser coupled to a mono-mode fiber optic was used. The laser beam is then directed to a cylindrical lens (f = 75mm) to form the light sheet. The illumination power was 40mw.

The collection path is composed of a Nikon PLAN FLUOR 10x NA = 0.28 mounted to the pupil segmentation module. The Vflat of the lens inside the pupil segmentation module was measured and saved before leaving from Padova following the procedure in Appendix **??**, in order to do not introduce aberrations when the lens is mounted after the objective. A manual translator is then placed in order to focus the objective lens to the plane formed by the light sheet. The final image is captured by a uEye CP3060 camera (1920x1200px) with a pixel size of 5.86µm using a Nikon tube lens (f = 200mm) and a long pass filter that cuts all the light with a wavelength below 540nm.

The sample we chose to scan are fluorescent beads emitting with a $\lambda = 565nm$ immersed in phytagel contained in a couvette surrounded by water and it can be moved in a direction parallel to the optical axis of the objective using a motorized translation stage (PI, M-405.CG) to obtain a 3-D image stack.

The setup scheme is shown in figure 6.2.

6.2 MEASURES WITH THE LIGHT SHEET FIXED

Given the fact that fluorescent light is very weak we set the camera to it's maximum gain and to a frame-rate of 3FPS, so the maximum exposure time is approximately 0.33s.

6.2.1 Calibration of the Lens

After that, the first thing we made was a calibration of the lens, shown in figure 6.3, and we immediately noticed that actuator #16 was not working. The most probable cause is that the soldered wire to the piezoelectric actuator has been unsoldered during the transport.

This will inevitably cause a loss of dynamic range in the correction stage and an initial aberration due to a not corrected initial configuration of the lens actuators.

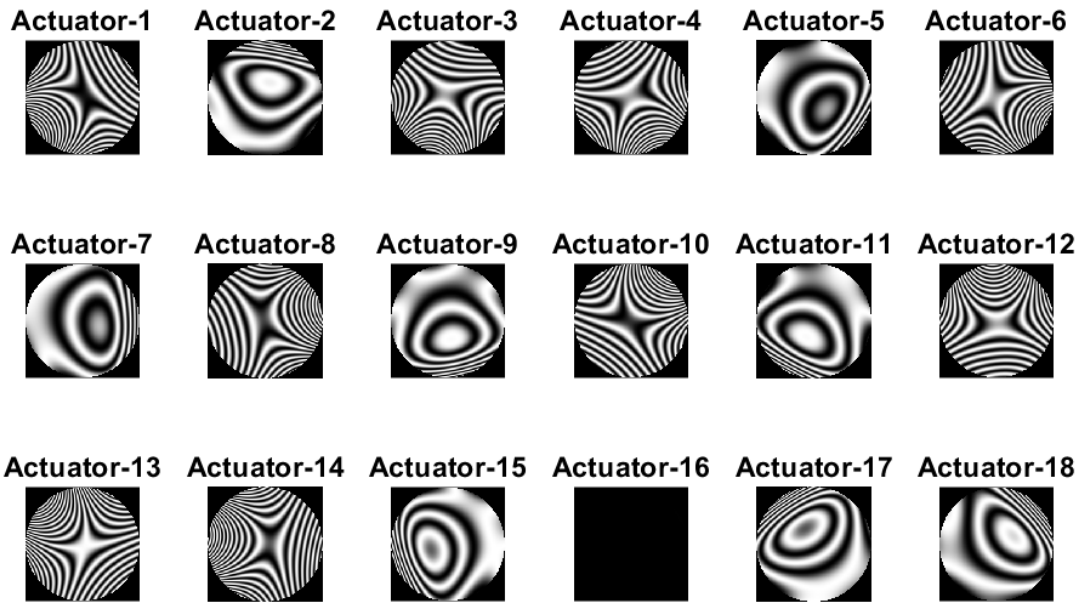

Figure 6.3.: Interferogram of the actuators response

Since the lens introduce an aberration, we have no direct way to measure the wavefront of the system without the adaptive lens, so to check the effectiveness of the correction system we can only compare the sample image taken with the correction using the

pupil segmentation correction system to the image taken without the pupil segmentation module.

6.2.2 Wavefront Measurement and Correction

We then proceeded with the measurement of the wavefront with the VFlat applied to the lens. This of course will have two contributions for the aberrations:

- the one from the system sample-objective-tube lens
- the one from the adaptive lens

and, as already stressed, we have no way to decouple the one from the other.

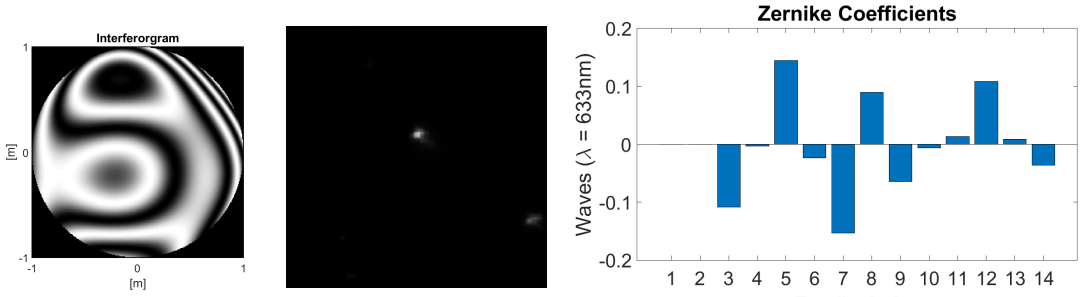

(a) Interferogram (b) Image of a bead (c) Zernike Coefficients

Figure 6.4.: Wavefront measurement with VFlat applied
RMS Wavefront Error: 0.29λ

In figure 6.7(c) we can see that the main aberrations are astigmatisms, coma and spherical aberration. The image of the beads is stretched and shows a lack of contrast.

We chose to perform a correction with three iterations with the results shown here below.

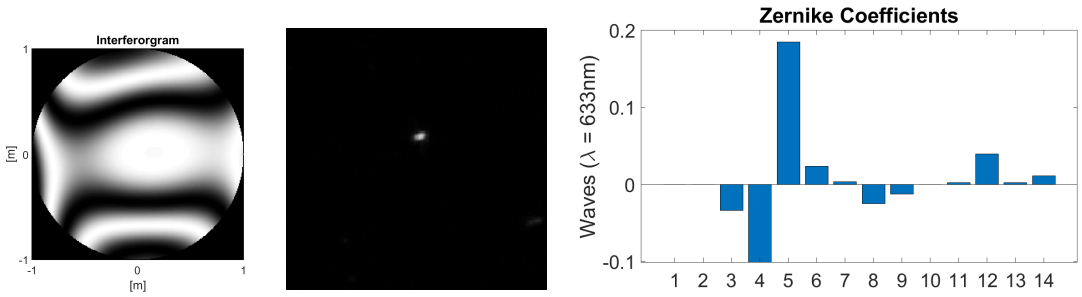

(a) Interferogram (b) Image of a bead (c) Zernike Coefficients

Figure 6.5.: Wavefront measurement after first correction
RMS Wavefront Error: 0.22λ

We can see that already after the second iteration, I was able to achieve diffraction limited results. We can compare now a wide field image with the lens after the correction and without the lens to see if the correction system can effectively improve image quality.

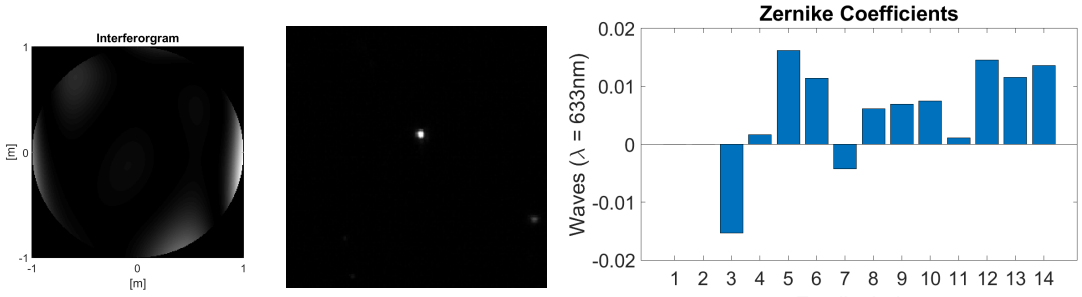

(a) Interferogram (b) Image of a bead (c) Zernike Coefficients

Figure 6.6.: Wavefront measurement after second correction
RMS Wavefront Error: 0.04λ

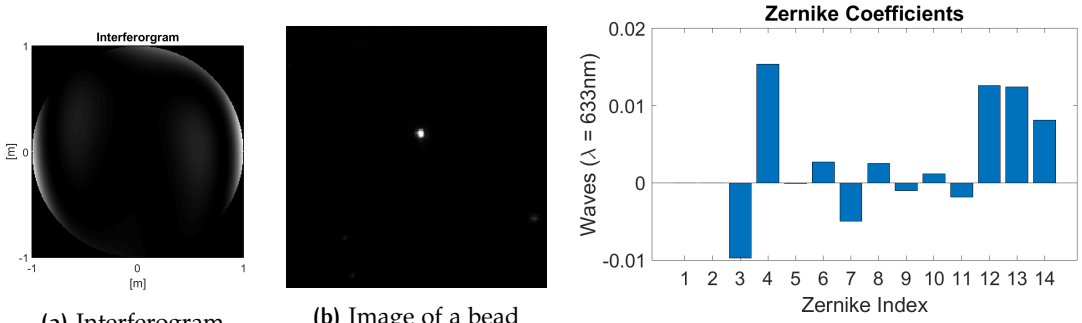

(a) Interferogram (b) Image of a bead (c) Zernike Coefficients

Figure 6.7.: Wavefront measurement after third correction
RMS Wavefront Error: 0.03λ

The correction is made considering the center portion of the image and we can see that using the pupil segmentation correction module the image has more contrast and the signal is greater, but there are two thing to notice:

- to obtain an image without the lens, we had to unscrew the lens and the objective, so the portion of the image taken with the lens is not the same compared to the image taken without the lens.
- if we focus our attention on a portion of the image away from the center, we can see that some aberration remains (see figure 6.9). This is because the system has an isoplanatic patch smaller than the camera sensor, and we are able to see portions of the image outside it.

6.3 3D IMAGE STACK

One of the main advantages of light sheet microscopy, is the ability to obtain 3D stacks of the image thanks to it's good optical sectioning.

In order to obtain an isotropic sectioning we need to set the motorized translator to a speed such that in the sectioning rendering we obtain a cubic voxel (volumetric pixel).

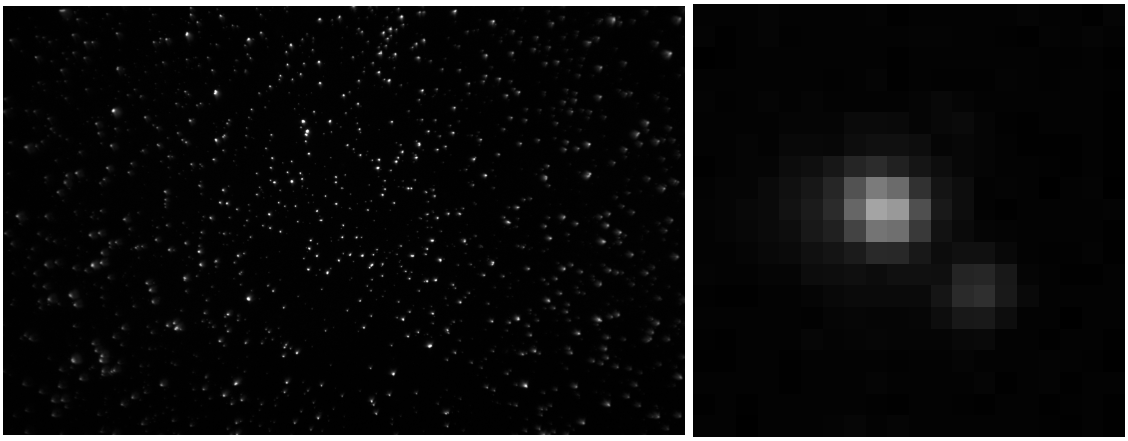

(a) Widefield Image After Correction

(b) Crop

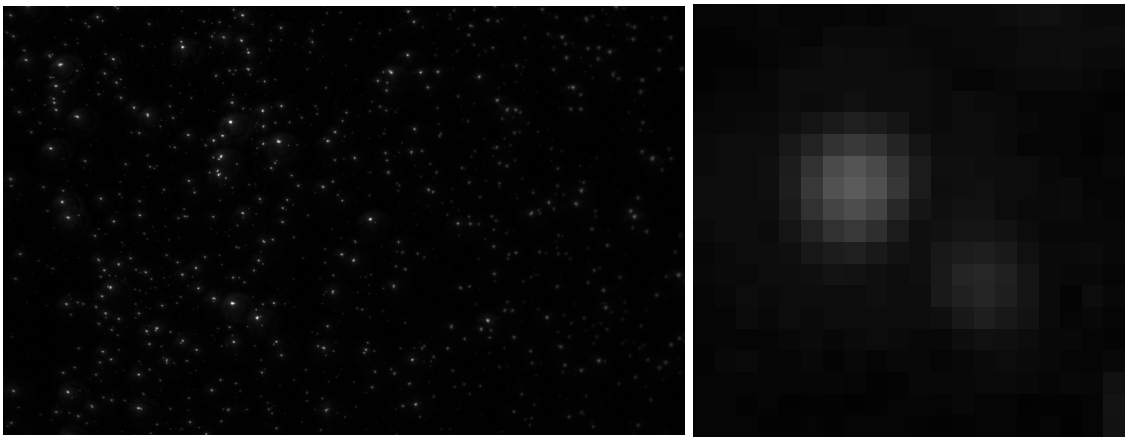

(c) Widefield Image with no adaptive lens

(d) Crop

Figure 6.8.: Comparison of the corrected image (top) with the image in absence of the adaptive lens (bottom). The improvement in signal and resolution is noticeable

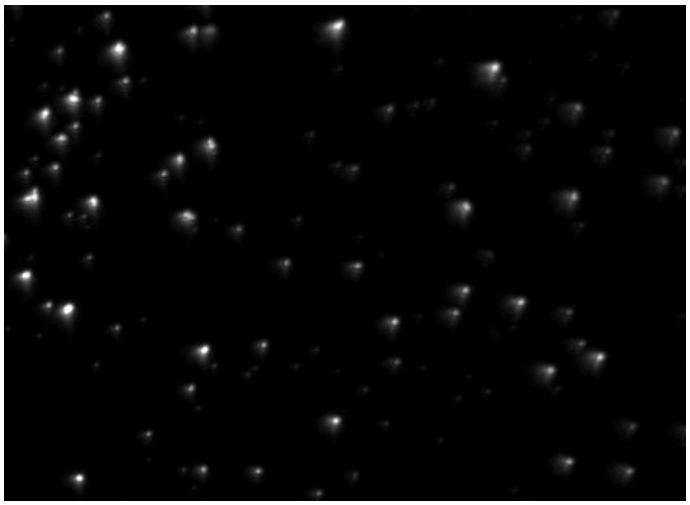

Figure 6.9.: Corner portion of the corrected image. From the shape of the beads we can deduce that the region outside the isoplanatic patch is affected by coma

First we set the camera for a good exposition of the beads:

Exp: 77.89ms, 12.87FPS, gain 40%

Given the 10x magnification, 1µm in the image plane correspond to 0.1µm in the object plane. The camera we used has a pixel size of 5.86µm that correspond to 586nm in object space. So we need to move the sample of 586nm every frame. We set the speed of the motorized translator to $586\text{nm} \cdot 12.87\text{Hz} = 7,5418\mu\text{m/s}$.

We then acquired a set of 250 frames, equal to 1.886mm of depth for both the case of the image corrected using the pupil segmentation module and the image in absence of the pupil segmentation module.

I then processed the images in ImageJ. The 3D rendering in the case of the images corrected using the PS module can be seen in figure 6.10.

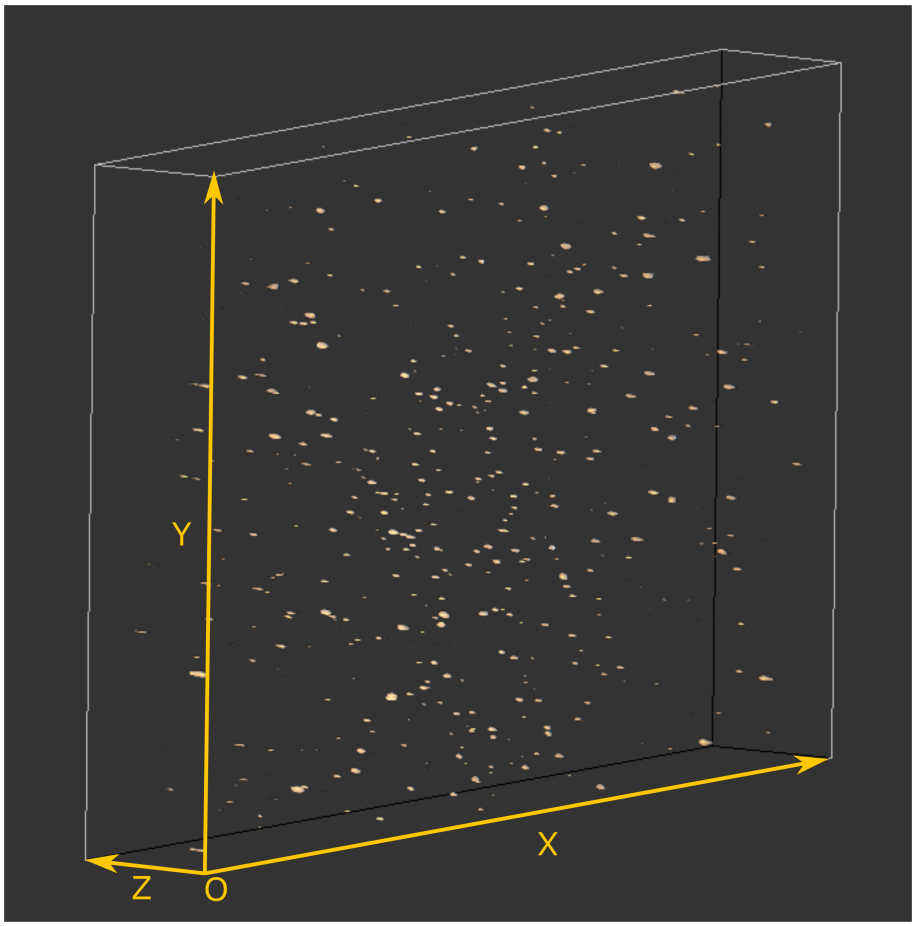

Figure 6.10.: 3D rendreing of the stacked images taken at various depths

A standard way to evaluate optical quality is to measure the lateral ($x - y$) or axial(z) width of the beads.

Considering the $x - z$ projection I took a portion of the image that in order to consider the image of a single bead for both the corrected image and the one taken with no adaptive lens.

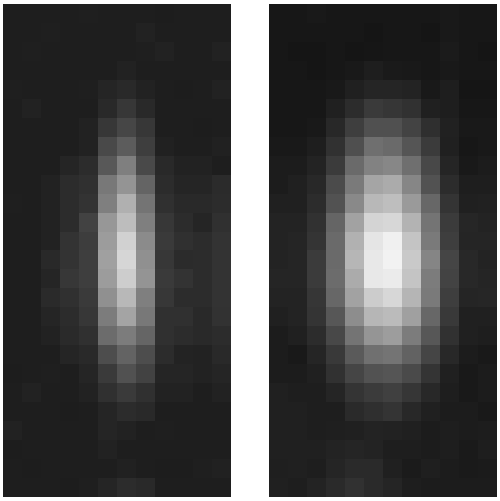

Figure 6.11.: $x - z$ section of one bead after the correction (left) and with no adaptive lens (right) (Intensity is normalized)

I then considered the x and z section respectively and I made a Gaussian fit. We can then link the sigma obtained from the fit of the bead intensity to the resolution of the optical system[18].

We can see the results in figure 6.12 and in table 6.1.

The diffraction limited resolution in the $x - y$ plane is given by the Abbe criterion 2.10 and is equal to $1.01\mu m$.

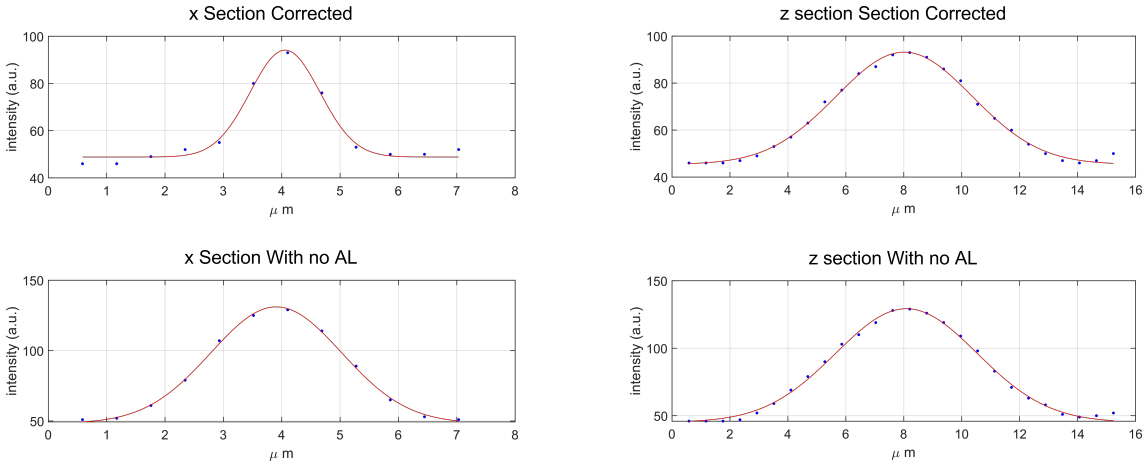

Figure 6.12.: Fit of the x and z section of the image of a bead taken with the correction using the AL (top) and without the AL (bottom)

	resolution x	**resolution z**
Corrected	$1.4 \pm 0.2\mu m$	$5.6 \pm 0.3\mu m$
No Lens	$2.7 \pm 0.1\mu m$	$5.8 \pm 0.3\mu m$
Diffraction limit	$1.01\mu m$	$5.3\mu m$

Table 6.1.: Resolution obtained from the fit of the x and z sections

6.4 DISCUSSION OF THE RESULTS

This results confirmed the capability of the system for correct for aberrations even in a more complex microscopic system such as a light sheet microscope and we were able to recover a diffraction limited resolution in the $x - y$ plane.

We then tried to apply this correction system to a zebrafish brain, a typical biological sample. However we were not able to measure (therefore correct) the wavefront because of the low level of fluorescence light of the sample combined with the loss of intensity due to the obstruction of the pupil during the wavefront measurement process.

7 CONCLUSIONS

Results Achieved

In this thesis I achieved some important results:

- In chapter 4 I showed that is possible to use a deformable lens to correct up until 0.5λ RMS of spherical aberration in a microscope setup.
- In chapter 5we implemented a module for microscopes that includes a deformable lens and the pupil segmentation technique.

  The module was installed on a bright field microscope. I showed that it is possible to use it to restore diffraction limited results in a scenario where some aberrations typical of a biological microscope setup were induced.

  The correction process takes less than a minute. Moreover, I showed that it is possible to carry out large field of view correction beyond the isoplanatic patch. For this purpose we implement a multi zone correction followed by stitching of the acquired images.
- After this initial phase of testing we applied this technique on state of the art light sheet microscope developed for biological studies. The experiments were carried out at the "Politecnico" of Milan where the microscope has been developed. The PS module has shown to be capable of correcting for aberrations induced by the system in this microscope setup in the case of imaging fluorescent beads. Thanks to the compactness of this device, the integration has been possible almost seamlessly, with no change in the optical path. This initial successful result opens the door to the possibility of using this technique in this same setup for the study of others biological samples.

Limitations

One of the most severe limitations of this technique is the loss of light during the measurement process due to the occlusion of the pupil aperture.

This limitation is reflected consequently in the number of sampling point. In fact, if we would need a higher sampling of the wavefront we would inevitably rise the number of apertures, diminishing the diameter of each of them. This can be a problem in microscopy when imaging samples with a weak fluorescence emission.

Further Improvements and Applications

With the recent developments of super resolution microscopy techniques Adaptive Optics will play in the future a very important role.

Therefore, the development of a easy to use adaptive optics module compatible with any microscope will be very useful to spread the use of Adaptive Optics in biological laboratories.

A DERIVATION OF FORMULA 2.11

Let's consider the case displayed in figure A.1 where a ray is focused by an objective lens to a point P and faces a refractive index mismatch (l_2).

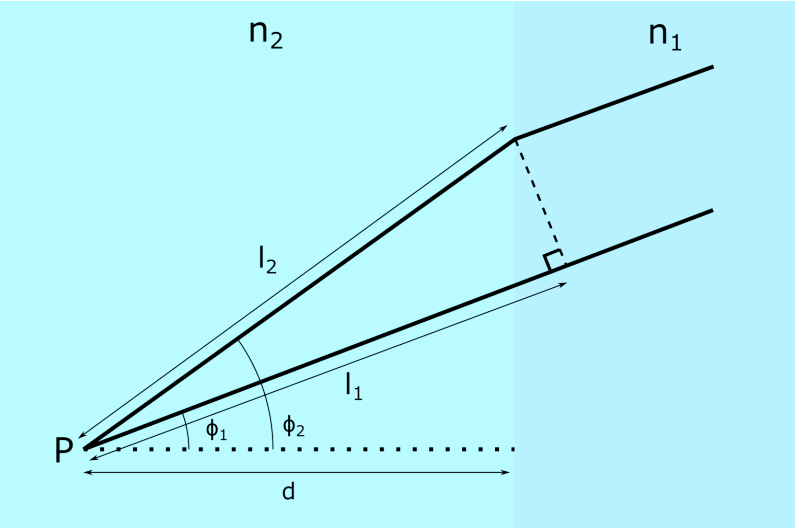

Figure A.1.

If we consider the case of a ray, always focused to P, but that does not faces the refractive index mismatch (i.e. it sees only n_1), the optical path difference is:

$$OPD = n_2 l_2 - n_1 l_1 \tag{A.1}$$

If we remember, the aberration function 2.1 $W(\xi,\eta)$ is an optical path difference in units of wavelength λ, so:

$$W = \frac{1}{\lambda}(n_2 l_2 - n_1 l_1) \tag{A.2}$$

and clearly W at this moment depends on, ϕ_1, ϕ_2, d, n_1 and n_2.

Using easy trigonometric considerations and remembering the Snell laws we have:

$$\begin{aligned} l_2 &= \frac{d}{\cos\phi_2} \\ l_1 &= l_2\cos(\phi_2 - \phi_1) \\ n_1 \sin\phi_1 &= n_2 \sin\phi_2 \end{aligned}$$

end we can rewrite W :

$$\begin{aligned}
W &= \frac{1}{\lambda}(n_2 l_2 - n_1 l_1) \\
&= \frac{1}{\lambda}\left(\frac{d}{\cos\phi_2} n_2 - n_1 l_2 \cos(\phi_2 - \phi_1)\right) \\
&= \frac{d}{\lambda}\left(\frac{n_2}{\cos\phi_2} - \frac{n_1}{\cos\phi_2}\cos(\phi_2 - \phi_1)\right) \\
&= \frac{d}{\lambda}\left(\frac{n_2}{\cos\phi_2} - \frac{n_1}{\cos\phi_2}(\cos\phi_2\cos\phi_1 + \sin\phi_2\sin\phi_1)\right) \\
&= \frac{d}{\lambda}\left(\frac{n_2}{\cos\phi_2} - n_1\cos\phi_1 - n1\sin\phi_1\frac{\sin\phi_2}{\cos\phi_2}\right) \\
&= \frac{d}{\lambda}\left(\frac{n_2}{\cos\phi_2} - n_1\cos\phi_1 - n2\frac{\sin^2\phi_2}{\cos\phi_2}\right) \\
&= \frac{d}{\lambda}\left(\frac{n_2 - n_2(1-\cos^2\phi_2)}{\cos\phi_2} - n_1\cos\phi_1\right) \\
&= \frac{d}{\lambda}(n_2\cos\phi_2 - n_1\cos\phi_1) \\
&= \frac{d}{\lambda}\left(n_2\sqrt{1-\sin^2\phi_2} - n_1\sqrt{1-\sin^2\phi_1}\right) \\
&= \frac{d}{\lambda}\left(\sqrt{n_2^2 - n_2^2\sin^2\phi_2} - \sqrt{n_1^2 - n_1^2\sin^2\phi_1}\right) \\
&= \frac{d}{\lambda}\left(\sqrt{n_2^2 - n_1^2\sin^2\phi_1} - \sqrt{n_1^2 - n_1^2\sin^2\phi_1}\right)
\end{aligned}$$

Now if we denote with α the maximum acceptance angle of the objective lens used in the medium with the refractive index n_1 and β the maximum acceptance angle of the objective lens used in the medium with the refractive index n_2, we have by it's definition that:

$$NA = n_1\sin\alpha = n_2\sin\beta$$

and we can write (collecting $n_1\sin\alpha$):

$$\begin{aligned}
W &= \frac{d}{\lambda} n_1\sin\alpha\left(\sqrt{\frac{n_2^2 - n_1^2\sin^2\phi_1}{n_1^2\sin^2\alpha}} - \sqrt{\frac{1-\sin^2\phi_1}{\sin^2\alpha}}\right) \\
&= \frac{d}{\lambda} n_1\sin\alpha\left(\sqrt{\frac{n_2^2}{n_2^2\sin^2\beta} - \frac{\sin^2\phi_1}{\sin^2\alpha}} - \sqrt{\frac{n_1^2}{n_1^2\sin^2\alpha} - \frac{\sin^2\phi_1}{\sin^2\alpha}}\right)
\end{aligned}$$

Defining the normalized radius $\rho \equiv \frac{\sin\phi_1}{\sin\alpha}$ we can write.

$$W(\rho) = \frac{d\ NA}{\lambda}\left(\sqrt{\left(\frac{n_2}{NA}\right) - \rho^2} - \sqrt{\left(\frac{n_1}{NA}\right) - \rho^2}\right) \tag{A.3}$$

BIBLIOGRAPHY

[1] E. Hecht, *"Optics"* (5^{th}ed.), Pearson (2017).

[2] M. Born and E. Wolf, *"Principles of Optics"*, 7^{th} expanded edition, Cambridge University Press (2000).

[3] A. Horst, *"High-refractive index particles in counter-propagating optical tweezers-manipulation and forces"*, Diss. Utrecht University (2006).

[4] Yao Xin-Cheng, Li Zhao-Lin, Guo Hong-Lian, Cheng Bing-Ying, Zhang Dao-Zhong, *"Effects of Spherical Aberration on Optical Trapping Forces for Rayleigh Particles"*, Chinese Physics Letters, Vol. 18, N. 3, 432-434, (2001).

[5] M.J. Booth, M.A.A. Neil, T. Wilson, *"Correction for Confocal Imaging in Refractive Index Mismatched Media"*, J. Microsc., Vol. 192, Pt. 2, 90-98, (1998).

[6] L. Silvestri, L. Sacconi, F.S. Pavone, *"Correcting Spherical Aberrations in Confocal Light Sheet Microscopy: A Theoretical Study"*, Microscopy research and technique 77(7), 483–491 (2014).

[7] H.W. Babcock, *"The possibility of compensating astronomical seeing"*, Publications of the Astronomical Society of the Pacific, 65 (386): 229–236 (1953).

[8] M. J. Booth, *"Adaptive optics in microscopy"* Philosophical Transactions of the Royal Society A: Mathematical, Physical and Engineering Sciences. 365 (1861): 2829–2843 (2007).

[9] K. Greger, J. Swoger, E. H. K. Stelzer *"Basic building units and properties of a fluorescence single plane illumination microscope"*, Rev. Sci. Instrum. 78, 023705 (2007).

[10] R.A. Muller, A. Buffington , *"Real-time correction of atmospherically degraded telescope images trough image sharpening"*, J. Opt. Soc. Am., 64(9), 1200-1210, (1974)

[11] N. Ji, D. E. Milkie, E. Betzig *"Adaptive optics via pupil segmentation for high-resolution imaging in biological tissues"*, Nature Methods. 7, 141 (2009).

[12] E. Paris, *La tecnica della Pupil-Segmentation*, tesi di laurea, Università degli studi di Padova, (2018), supervisor S. Ortolani, co-supervisors S.Bonora and M. Quintavalla.

[13] Stefano Bonora, Yifan Jian, Pengfei Zhang, Azhar Zam, Edward N. Pugh, Robert J. Zawadzki, and Marinko V. Sarunic, *"Wavefront correction and high-resolution in vivo OCT imaging with an objective integrated multi-actuator adaptive lens"* Opt. Express 23, 21931-21941 (2015)

[14] L. Rizzotto, *Confocal Microscopy with Sensorless Adaptive Optics*, tesi di laurea, Università degli studi di Padova, (2014), supervisor S. Bonora, co-supervisor F.Mammano.

[15] L. Sherman, J. Y. Ye, O. Albert and T. B. Norris, "Adaptive correction of depth-induced aberrations in multiphoton scanning microscopy using a deformable mirror". Journal of Microscopy, 206: 65-71, (2002).

[16] H. Itoh, N. Matsumoto, and T. Inoue, *"Spherical aberration correction suitable for a wavefront controller"*, Opt. Express 17, 14367-14373, (2009).

[17] A. Candeo, I. Sana, E. Ferrari, C. D'Andrea, L. Maiuri, G. Valentini, A. Bassi, *"Virtual unfolding of light sheet fluorescence microscopy dataset for quantitative analysis of the mouse intestine"*, J. of Biomedical Optics, 21(5), 056001 (2016).

[18] B. Zhang, J. Zerubia, J. C. Olivo-Marin, *"Gaussian approximations of fluorescence microscope point-spread function models"*, Appl. Opt. 46, 1819-1829 (2007)